



저작자표시-비영리-변경금지 2.0 대한민국

이용자는 아래의 조건을 따르는 경우에 한하여 자유롭게

- 이 저작물을 복제, 배포, 전송, 전시, 공연 및 방송할 수 있습니다.

다음과 같은 조건을 따라야 합니다:



저작자표시. 귀하는 원저작자를 표시하여야 합니다.



비영리. 귀하는 이 저작물을 영리 목적으로 이용할 수 없습니다.



변경금지. 귀하는 이 저작물을 개작, 변형 또는 가공할 수 없습니다.

- 귀하는, 이 저작물의 재이용이나 배포의 경우, 이 저작물에 적용된 이용허락조건을 명확하게 나타내어야 합니다.
- 저작권자로부터 별도의 허가를 받으면 이러한 조건들은 적용되지 않습니다.

저작권법에 따른 이용자의 권리는 위의 내용에 의하여 영향을 받지 않습니다.

이것은 [이용허락규약\(Legal Code\)](#)을 이해하기 쉽게 요약한 것입니다.

[Disclaimer](#)

이학박사 학위논문

**Heteroepitaxial manipulation of
oxygen octahedral rotation and
associated physical properties**

산소 팔면체 회전 및 관련 물성의
이종에피택시 제어

2021년 2월

서울대학교 대학원

물리천문학부

김정래

Heteroepitaxial manipulation of oxygen octahedral rotation and associated physical properties

Jeong Rae Kim

Supervised by

Professor Tae Won Noh

A Dissertation submitted to the Faculty of Seoul National
University in Partial Fulfillment of the Requirements for the
Degree of Doctor of Philosophy

February 2021

Department of Physics and Astronomy

Graduate School

Seoul National University

Heteroepitaxial manipulation of oxygen octahedral
rotation and associated physical properties

산소 팔면체 회전 및 관련 물성의 이종에피택시 제어

지도교수 노 태 원

이 논문을 이학박사학위논문으로 제출함

2020 년 12 월

서울대학교 대학원

물리천문학부

김 정 래

김정래의 박사학위논문을 인준함

2021 년 1 월

위 원 장	차 국 린	(인) 
부 위 원 장	노 태 원	(인) 
위 원	민 흥 기	(인) 
위 원	김 기 훈	(인) 
위 원	양 상 모	(인) 

Abstract

The rotation of oxygen octahedron is a fundamental structural distortion in a group of materials called perovskite oxides. The oxygen octahedral rotation (OOR) allows the perovskite oxides to accommodate a variety of transition metal ions, generating a rich spectrum of correlated electronic phases. In these correlated electron systems, the strong interplay between charge, spin, orbital, and lattice degrees of freedom makes the OOR a decisive factor when investigating the associated physics. Moreover, it implies that the controlled manipulation of the OOR leads to the highly tunable physical properties of the transition metal oxides (TMOs). This dissertation experimentally demonstrates the manipulation of the OOR and the associated physical properties in epitaxial perovskite oxide heterostructures.

Artificial heterostructures composed of perovskite oxide have brought about a wide range of emergent phenomena and functionalities. This versatile platform largely originates from the high integrability of the ABO_3 perovskite structure which can form a well-defined interface with the other. Since the OOR is a collective motion of three-dimensionally connected octahedron, substantial octahedral connectivity is expected at the oxide interfaces. Here, we exploit the interfacial octahedral connectivity to control the OOR, thus realizing novel ferroelectricity and tunable electronic structures.

There can be 23 possible patterns of the OORs, but only a few OOR patterns are predominantly present as bulk crystals. This has restricted the range of possible properties and functions of perovskite oxides, necessitating the utilization of nonequilibrium OOR patterns. we demonstrate that a designed metastable OOR pattern leads to robust room-temperature ferroelectricity in CaTiO_3 , which is otherwise paraelectric in equilibrium. Based on density functional theory, we surveyed 10 possible nonequilibrium OOR pattern of CaTiO_3 and found a metastable OOR pattern which is cooperative with ferroelectricity. We stabilized the target OOR pattern of CaTiO_3 using the geometric design of epitaxial heterostructures. Atomic-scale imaging combined with deep neural network analysis confirms a close correlation between the metastable OOR pattern and electric polarization. The attained electric polarization was switchable and stable at room-temperature, demonstrating that manipulation of OOR pattern can create unconventional ferroelectric materials.

Despite the tremendous interest on the electronic structures at the oxide interfaces, no direct experimental probe has been made. To manifest how the oxide interfaces modify the electronic structure, we necessitate a proper experimental platform to explore the phenomena. Conceiving that such interfacial effect would has limited length scale, we first search for an atomically thin and electronic TMO heterostructure.

In the experimental reports so far, the TMO thin films have become insulating when confined to a single-atomic-layer thickness. This is not only because the electronic phases are intrinsically insulating, but also because of the experimental difficulties of maintaining the metallic phases down to monolayer limit. Combining atomic-scale

control of epitaxy and angle-resolved photoemission spectroscopy, we discovered that the monolayer SrRuO₃ is a strongly correlated metal. Our systematic investigation reveals a close correlation between the electronic phase and magnetism.

After clarifying the electronic structures of the SrRuO₃ films down to monolayer, we experimentally demonstrate the interface control of electronic structure at the TMO heterostructures. We employed insulating buffer layers of BaTiO₃, SrTiO₃, and CaTiO₃ which impose different structural symmetries to the SrRuO₃ layers. Above two monolayer thickness, no significant change has been observed in the electronic structures of SrRuO₃ films. However, at the two and one monolayer thickness, substantial modification of the electronic structure has been made. In the monolayer limit, the two-dimensional electronic structures have crossover between Fermi-liquid, Hund's metal, and antiferromagnetic Mott insulators.

Keywords: perovskite oxide, oxygen octahedral rotation, correlated electron system, oxide heterostructure, pulsed laser deposition, ferroelectricity, electronic structure

Student number: 2015-20322

Abstract

Contents

List of Figures

1	Introduction.....	1
1.1	Octahedral rotation in perovskite oxides.....	1
1.2	Oxygen octahedral rotation in correlated electron systems.....	2
1.3	Heteroepitaxial manipulation of oxygen octahedral rotation.....	7
2	Fabrication of epitaxial oxide heterostructures.....	10
2.1	Preparation of perovskite oxide substrates.....	10
2.1.1	atomically flat and singly terminated substrates for constructing epitaxial oxide heterostructures.....	10
2.1.2	Experimental methods.....	13
2.1.3	Thermal annealing.....	15
2.1.4	Chemical etching.....	20
2.1.5	Surface termination analysis by ion scattering spectroscopy.....	23
2.1.6	Possible surface structures of LaAlO ₃ (001) substrates after water leaching.....	26
2.1.7	Fabrication of an abrupt oxide heterointerface on LaAlO ₃ (001) surfaces.....	28
2.1.8	Other substrates.....	30
2.2	Pulsed laser deposition of epitaxial oxide heterostructures.....	31
2.2.1	Pulsed laser deposition.....	31

2.2.2	Parameters of pulsed laser deposition.....	34
2.2.3	Optimization of high-quality perovskite oxide thin films.....	35
2.3	Summary.....	37
3	Stabilizing hidden room-temperature ferroelectricity via a metastable atomic distortion pattern.....	41
3.1	Background.....	42
3.1.1	Pattern of oxygen octahedral rotation (OOR).....	42
3.1.2	Ferroelectricity.....	44
3.1.3	Structural coupling between OOR and ferroelectricity.....	45
3.2	Experimental methods.....	46
3.2.1	Growth and characterization of thin films.....	46
3.2.2	Piezoresponse force microscopy (PFM).....	48
3.2.3	Density functional theory (DFT) calculation.....	48
3.2.4	Second harmonic generation (SHG).....	49
3.2.5	Scanning transmission electron microscopy (STEM).....	50
3.3	Results and Discussion.....	50
3.3.1	Theoretical survey on nonequilibrium octahedral rotation pattern.....	50
3.3.2	Heteroepitaxial stabilization of metastable octahedral rotation pattern...53	
3.3.3	Atomic-scale visualization of oxygen octahedral rotation.....	56
3.3.4	Switchable and stable polarization at room-temperature.....	61
3.3.5	Discussion.....	64
3.4	Summary.....	65

4	Demonstration of controllable electronic structures at oxide heterointerfaces..	69
4.1	Background.....	70
4.1.1	Emergent phenomena at oxide interfaces.....	70
4.1.2	Metal-insulator transition in ultrathin oxide films.....	71
4.1.3	Motivation.....	72
4.2	Observation of a metallic single-atomic-layer oxide.....	73
4.2.1	Design of charging-free ultrathin SrRuO ₃ heterostructures.....	76
4.2.2	Thickness-dependent electronic structures of ultrathin SrRuO ₃ films....	79
4.2.3	Electronic coherency and magnetism in ultrathin SrRuO ₃ films.....	82
4.2.4	Interplay between dimensionality, electronic correlation, and magnetism.....	85
4.2.5	Charge modulation of the monolayer SrRuO ₃	86
4.3	Interface control of electronic structures in ultrathin oxide heterostructures..	89
4.3.1	Interface control of octahedral distortion.....	89
4.3.2	Crossover between Mott insulator, incoherent metal, and Fermi liquid in the monolayer SrRuO ₃	91
4.4	Summary.....	93
5	Conclusion.....	96

Publication List

국문 초록 (Abstract in Korean)

감사의 글 (Acknowledgements)

Chapter 1

Introduction

1.1 Octahedral rotation in perovskite oxides

Perovskite oxide has a chemical formula of ABO_3 whose structure is cubic or pseudo-cubic. The basic building block of the perovskite oxide is the corner-sharing BO_6 octahedra, where the B-site cations are usually transition-metal ions. By distorting the BO_6 octahedra, the perovskite oxides can accommodate a variety of A- and B-site cations with different ionic radius, becoming one of the most abundant structural family of materials. The wide range of physical properties and functionalities has attracted considerable attention in contemporary condensed matter physics and materials science.

The oxygen octahedral rotation (OOR) is a fundamental structural distortion in the perovskite oxides [1]. Tolerance factor t is a value given by the ratio of bond lengths as formula below, and it represents structural instabilities in the perovskite oxides [2].

$$t = r_{A-O} / \sqrt{2} r_{B-O}$$

(r_{X-O} : X–O bond length)

When $t = 1$, all constituting ions barely touch each other and form ideal cubic perovskite structure. The $t < 1$ (> 1) indicates that A-site (B-site) cation is too small, or B-site (A-site) cation is too big. The $t < 1$ structural instability can be mediated by the OOR which reduce the A-O bond length [3]. In fact, most bulk perovskite oxides have relatively small A-site cation and, as a result, the OOR [4].

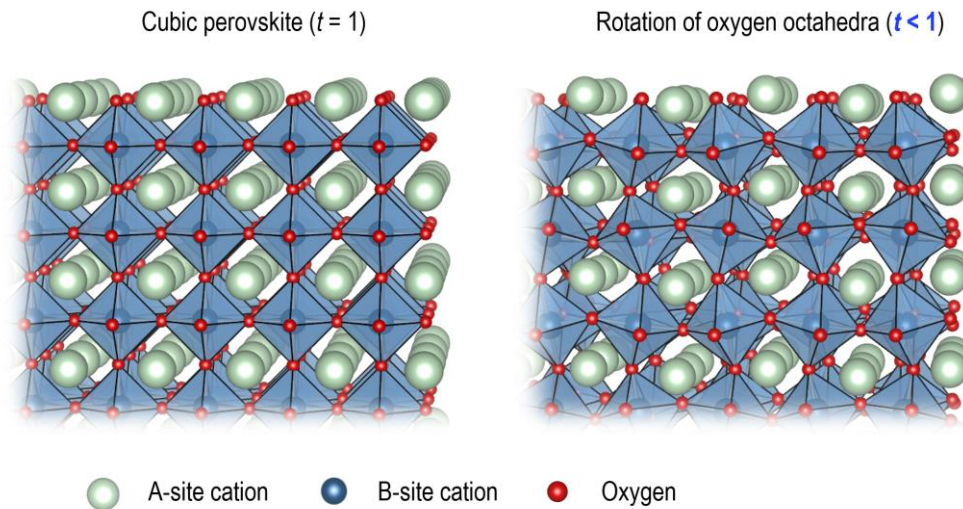


Figure 1.1. Structure stabilization by oxygen octahedral rotation in perovskite oxide.

1.2 Oxygen octahedral rotation in correlated electron systems

The transition metal oxides are classified as correlated electron systems in which their behavior cannot be described in terms of non-interacting particles. In the correlated electron systems, the strong interplay between charge, spin, orbital, and lattice degrees of

freedom is present [5-7]. Being one of lattice degrees of freedom, the angle and pattern of the OOR often played an important role in the correlated electron systems. A finite OOR angle reduce the B-O-B bond angle from the 180° of cubic perovskites. It subsequently reduces the overlap between B d -orbitals and O $2p$ -orbitals, weakening the nearest neighbor interactions. The OOR pattern are often related to the ordering of charge, spin, orbital, and lattice. We discuss several such cases.

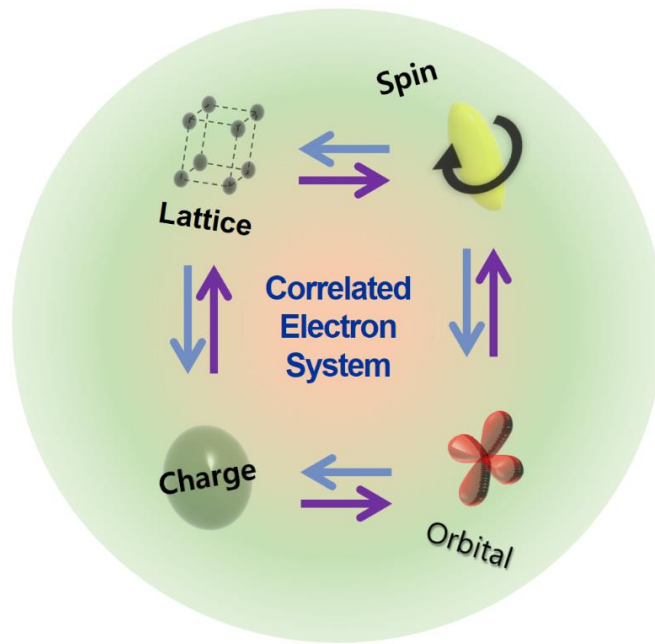


Figure 1.2. Schematic description of interplay between charge, spin, orbital and lattice degrees of freedom in correlated electron system.

The OORs of bulk perovskite oxides were often controlled through isovalent substitution of the A-site cations and application of hydrostatic pressure. In perovskite nickelates RNiO_3 (R = rare earth metal), the angle of OOR was systematically varied [8]. The increase of OOR angle reduces the Ni-O-Ni bond angle and consequently the electron hopping. As a result, the RNiO_3 undergoes a bandwidth-controlled metal-insulator transition as the OOR angle increases. It was shown that the insulating phases of RNiO_3 have bond disproportionation and G-type charge ordering of d^8L^2 and d^8L^0 NiO_6 octahedra [9].

The OOR can generate exotic magnetic states in some magnetic perovskite oxides. When two neighboring magnetic spins interact through oxygen, they usually align (anti-)parallel through magnetic exchange mechanism. When the two spins interact anti-symmetrically, the Dzyaloshinskii-Moriya interaction induces a spin canting [10]. The tilted B-O-B bonding in the presence of the OOR suffices the anti-symmetric exchange condition, becoming a source of weak ferromagnetism in antiferromagnets. For example, Perovskite manganese oxides AMnO_3 (A = Alkaline earth metal) have anti-ferromagnetic insulating phases. SrMnO_3 has undistorted cubic perovskite structure. As the Sr is substituted by Ca ($\text{Sr}_{1-x}\text{Ca}_x\text{MnO}_3$), the OOR gradually evolves and the weak ferromagnetic moments correspondingly emerges [11].

Certain symmetry allowed by a OOR pattern can determines the ordering of physical degrees of freedom. In particular, the type of orbital ordering in perovskite vanadates RVO_3 (R = rare earth metal) is largely dependent on the OOR, whose symmetry is orthorhombic [12]. The RVO_3 has $3d^2$ electronic configuration with low-temperature

ordering of d_{zx} and d_{yz} orbitals. Depending on the rare earth ion, the RVO_3 has a ground state orbital ordering of either G-type or C-type. This is due to a strong structural coupling between C-type ordering and the orthorhombic OOR pattern, so enhancing the OOR induces the transition from G-type to C-type orbital ordering [13].

The perovskite oxides possess various structural distortions such as the OOR, ferroelectricity, breathing distortion, Jahn-Teller distortion, and so on. Being a structural distortion, the OOR also interacts with the other structural distortions, in either cooperative or competitive way. For instance, the described charge and orbital orderings occur together with the breathing and Jahn-Teller distortion, respectively. The OOR is intimately related to the ferroelectric distortion as well, which will be discussed in chapter 3.

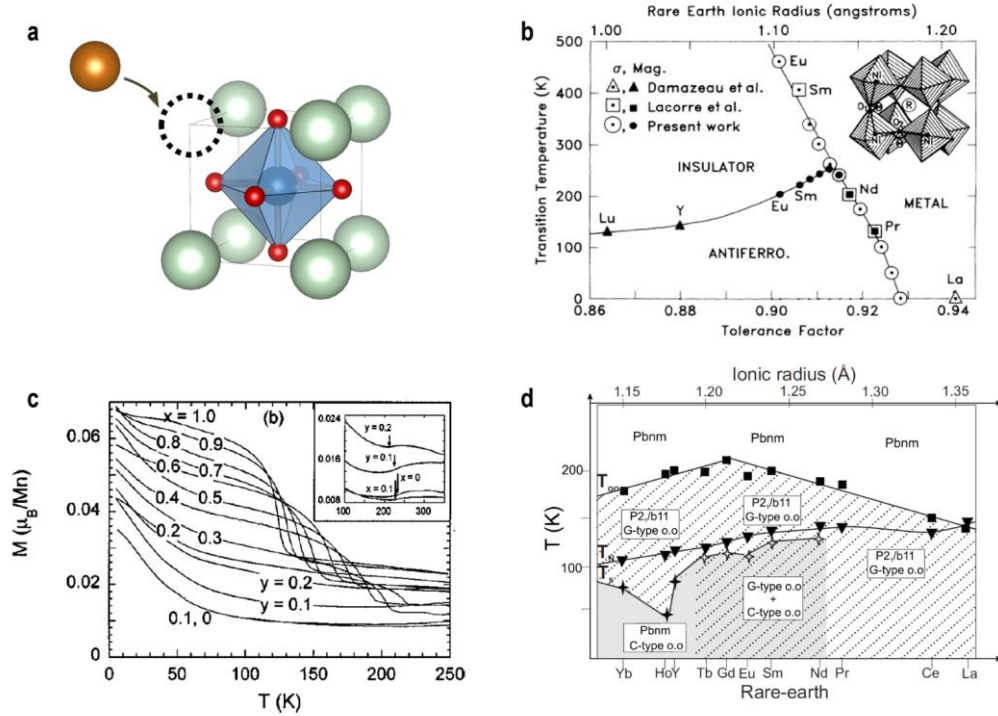


Figure 1.3. Control of oxygen octahedral rotation and associated charge, spin and orbital degrees of freedom. (a) Schematic description of bulk isovalent substitution of A-site cation. (b) Electronic phase diagram of $RNiO_3$ ($R =$ rare earth) depending on temperature and rare earth ion. (c) Doping-dependent magnetization of $Sr_{1-x}Ca_xMnO_3$. (d) Phase diagram of orbital ordering in RVO_3 ($R =$ rare earth) depending on temperature and rare earth ion. Adapted from [8,11,12].

1.3 Heteroepitaxial manipulation of oxygen octahedral rotation

The deterministic role of the OOR in the subtle interplay between charge, spin, orbital, and lattice degrees of freedom signifies that engineering the OORs are highly likely to realize novel phases of materials. However, conventional ways for controlling the OOR is limited by the choice of atoms and range of applicable pressure. In addition, some OOR patterns might be inaccessible at the given valence states of A- and B-site cations [14]. Much attention is being paid to developing effective means for the OOR engineering.

Another unique feature of the ABO_3 perovskite oxide is the three-dimensionally connected BO_6 octahedra. The simple structures, strong connectivity, and broad range of physical properties give rise to a remarkably useful platform for constructing artificial heterostructures [15]. Here, if two materials with different OOR structures form a heterojunction, the continuity condition at the interface will enforce the modulation of the OOR [16]. Using this interfacial octahedral connectivity, both angles and patterns of the OOR have been successfully modulated in various interfaces including $LaAlO_3/SrTiO_3$, $SrRuO_3/SrTiO_3$, $BiFeO_3/La_{0.7}Sr_{0.3}MnO_3$, and $NdNiO_3/LaAlO_3$ interfaces.

In this dissertation, we aim to explore novel phases of perovskite oxides by heteroepitaxially manipulating the OOR. We fabricate a high-quality epitaxial oxide heterostructures with atomically abrupt interfaces using pulsed laser deposition technique. Through engineering the angle and pattern of OOR, we can realize a novel room-temperature ferroelectricity out of bulk nonpolar $CaTiO_3$ and interfacial control of electronic phases in atomically thin $SrRuO_3$ films.

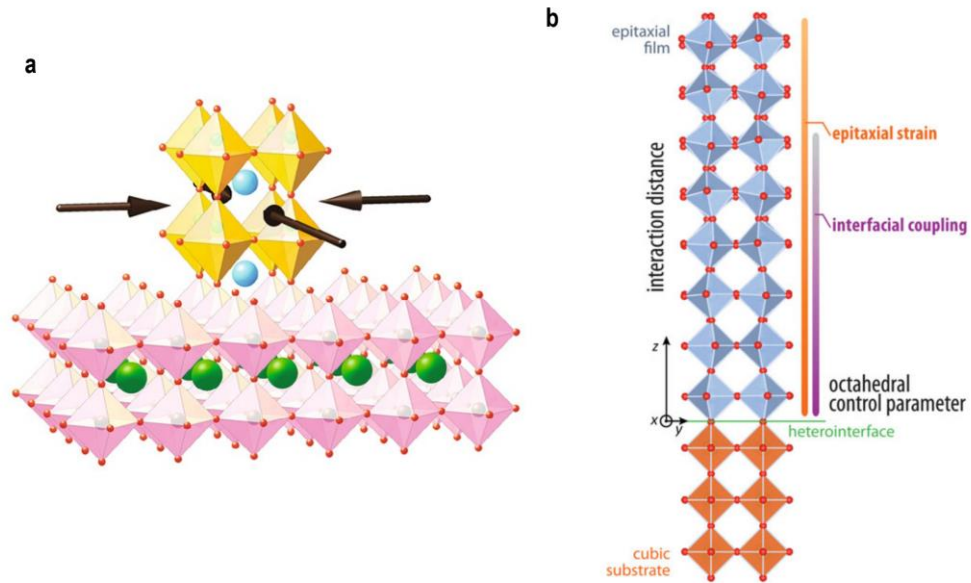


Figure 1.4 Schematic description of perovskite oxide heterostructures and structural control. (a) Strain engineering by lattice-mismatched substrate. (b) Control of octahedral rotation by interfacial octahedral connectivity. Adapted from [15,16].

References

- [1] A. M. Glazer, *Acta Cryst.* **B28**, 3384 (1972).
- [2] V. M. Goldschmidt, *Naturwissenschaften*, **14**, 477 (1926).
- [3] P. M. Woodward, *Acta Cryst.* **B53**, 44 (1997).
- [4] M. W. Lufaso and P. M. Woodward, *Acta Cryst.* **B57**, 725 (2001).
- [5] E. Dagotto, *Rev. Mod. Phys.* **66**, 763 (1994).
- [6] M. Imada, A. Fujimori, and Y. Tokura, *Rev. Mod. Phys.* **70**, 1039 (1998).
- [7] Y. Tokura and Y. Tomioka, *J. Magn. Magn. Mater.* **200**, 1 (1999).
- [8] J. B. Torrance, P. Lacorre, A. I. Nazzal, E. J. Ansaldo, and C. Niedermayer, *Phys. Rev. B* **45**, 8209 (1992).
- [9] R. J. Green, M. W. Haverkort, and G. A. Sawatzky, *Phys. Rev. B* **94**, 195127 (2016).
- [10] S.-W. Cheong and M. Mostovoy, *Nat. Mater.* **6**, 13 (2007).
- [11] O. Chmaissem, *et al.*, *Phys. Rev. B* **64**, 134412 (2001).
- [12] M. H. Sage, G. R. Blake, C. Marquina, and T. T. M. Palstra, *Phys. Rev. B* **76**, 195102 (2007).
- [13] J. Varignon, N. C. Bristowe, E. Bousquet, and P. Ghosez, *Sci. Rep.* **5**, 15364 (2015).
- [14] I. H. Inoue, *Semicond. Sci. Technol.* **20**, S112 (2005).
- [15] R. Ramesh and D. G. Schlom, *Nat. Rev. Mater.* **4**, 257 (2019).
- [16] J. M. Rondinelli, S. J. May, and J. W. Freeland, *MRS Bull.* **37**, 261 (2012).

Chapter 2

Fabrication of epitaxial oxide heterostructures

2.1 Preparation of perovskite oxide substrates

2.1.1 Atomically flat and singly terminated substrates for constructing epitaxial oxide heterostructures

A variety of intriguing physics and highly tunable functionalities were discovered at the interfaces of perovskite oxide heterostructures during the last two decades [1, 2]. In these active research fields based on complex oxide heterostructures, precise control of interfacial structure on an atomic level is of great importance. Specifically, by artificially manipulating atomic termination sequence, we can stabilize and tune interfacial structure and associated physical phenomena which do not exist in bulk compounds. Fascinating examples include two-dimensional electron gas at a $\text{LaAlO}_3/\text{SrTiO}_3$ heterointerface [3], surface-termination-dependent electronic properties of LaNiO_3 ultrathin films [4], interfacial control of ferroelectricity and tunneling conductance in ultrathin ferroelectric films [5-7], and interface dipole engineering of Schottky barrier [8].

Oxide heterostructures are usually grown epitaxially on single crystal substrates. Hence, an atomically flat, singly terminated substrate surface is indispensable for realizing sharp heterointerfaces. Such surfaces were first realized on SrTiO₃ (001) substrates. SrTiO₃ has a cubic perovskite structure with nominally non-polar SrO and TiO₂ layers alternating along the [001] crystallographic direction. Thanks to the distinct solubility of SrO and TiO₂ layers in acid, a uniformly TiO₂-terminated surface can be prepared via etching the SrTiO₃ substrate in buffered hydrofluoric acid [9, 10]. Subsequent thermal annealing forms a simple step-terrace structure with atomic-level roughness [11]. Therefore, atomically flat SrTiO₃ substrates have been widely used to fabricate various complex oxide heterostructures.

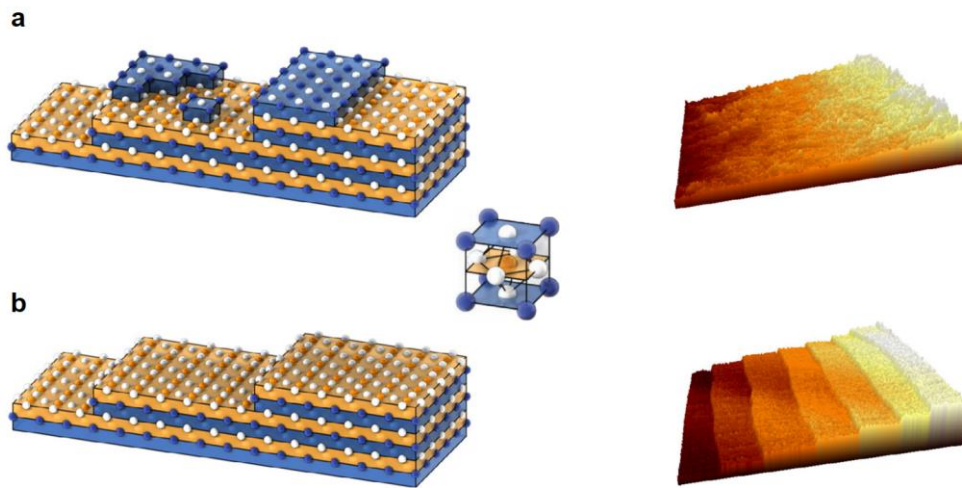


Figure 2.1 Surface structure of perovskite oxide single crystal substrate. (a) Rough, chemically inhomogeneous surface of as-received substrate. (b) Atomically flat, singly terminated surface of a well-prepared substrate. Adapted from [10].

In this chapter, using LaAlO_3 (001) as an example, we describe a method to prepare atomically flat and singly terminated oxide substrates. LaAlO_3 (LAO) single crystal is another commonly used perovskite substrate for oxide thin film growth. LAO has a smaller pseudo-cubic lattice constant (3.789 Å) than most of the perovskite-structured transition metal oxides. This feature makes LAO an ideal template for strain engineering [12]. For instance, tetragonal-phase BiFeO_3 can be epitaxially stabilized on an LAO(001) substrate with a compressive strain. [13]. The huge compressive strain between the film and the substrate ($\sim -4.5\%$) gives rise to the large tetragonality and enhanced ferroelectric polarization. In addition, unlike SrTiO_3 (001), the LAO(001) substrate has polar surfaces of LaO^+ or AlO_2^- . The polar surface can serve as a new electrostatic boundary condition and tune the electronic properties of epitaxial films [14, 15].

Despite such diverse use in oxide heterostructures, it is quite challenging to prepare an atomically flat and singly terminated LAO(001) surface. LAO can be conceptually viewed as a stack of alternating LaO^+ and AlO_2^- layers along the pseudo-cubic [001] direction. The polar nature of these layers makes the structure unstable due to the diverging Coulomb energy cost. Ideal LAO(001) surface therefore can easily reconstruct either structurally or electronically in high temperature. It has already been demonstrated experimentally that the conventional methods of post-annealing a chemically treated LAO(001) substrate can easily result in a mixed LaO and AlO_2 termination [16]. During the high-temperature ($> 930\text{ }^\circ\text{C}$) annealing process, a $\sqrt{5} \times \sqrt{5}$ La_4O_5 surface reconstruction can also occur, which impedes the formation of singly AlO_2^-

terminated LAO(001) surfaces [16, 17].

The preparation of atomically flat and singly terminated LAO(001) substrates consists of high-temperature thermal annealing and subsequent deionized water leaching processes. The evolutions of the surface morphology with respect to the annealing conditions and leaching times were visualized using atomic force microscopy (AFM). We found that the LaO component at the LAO(001) surface can be gradually dissolved in water. Using co-axial impact-collision ion scattering spectroscopy (CAICISS), we confirmed that the final LAO(001) surface is uniformly terminated with an AlO₂ layer. The AlO₂-terminated surface is highly stable, even at high temperature up to 700 °C. Using its robust surface stability, we demonstrate that we can epitaxially grow other complex oxide films with an atomically sharp heterointerface.

2.1.2 Experimental methods.

We used commercial LAO(001) single crystal substrates (Crystec GmbH) with a miscut angle of less than 0.1°. We prepared the atomically flat LAO(001) surface by thermal annealing and deionized water leaching. During the thermal annealing, LAO substrates were kept in a tube furnace under flowing oxygen at a flow rate of 0.5 L/min. The annealing was performed at 1,000, 1,100, or 1,200 °C for 3 hours. The annealed LAO substrates were then soaked in deionized water and sonicated for a particular time duration (t_w). We characterized the prepared LAO(001) surfaces using AFM (Cypher, Asylum Research) in ambient conditions. The spring constant, resonance frequency, and

tip radius of used AFM probes are ~ 40 N/m, ~ 300 kHz, and < 10 nm, respectively (Tap300Al-G, Budget Sensors).

We carried out CAICISS measurements on the treated LAO(001) substrates at room temperature in an ultrahigh vacuum chamber equipped with a CAICISS (TALIS-9700, Shimadzu) analyzer and a 2 keV He ion source. The background gas pressure was kept at $\sim 10^{-9}$ Torr. The ion scattering spectra were taken along the LAO [111] direction to identify the terminating layer of the crystals. The [111] direction of the crystals were identified by taking in-plane azimuth and out-of-plane polar angle scans of the He backscattering intensity and finding the symmetry point [18]. For an ideal perovskite structure, this would occur at an azimuth angle of 45° (along the in-plane [110] azimuth) and a polar angle of 35° from the crystal surface plane.

We grew SrRuO₃ (SRO) epitaxial film on atomically flat LAO(001) substrates using pulsed laser deposition (PLD). A polycrystalline SRO target was ablated with a KrF excimer laser at an energy density of 1.5 J/cm² and a repetition rate of 3 Hz. During film growth, the LAO substrate temperature and oxygen pressure were maintained at 700 °C and 100 mTorr, respectively. The interfacial atomic structures of the SRO/LAO(001) film was characterized by scanning transmission electron microscope (STEM, JEM-ARM200F, JEOL). The cross-sectional high-angle annular dark-field scanning transmission electron microscope (HAADF-STEM) image was taken along the LAO [100] zone axis.

2.1.3 Thermal annealing

First, we investigated the LAO(001) surface evolution under various thermal annealing conditions. We used AFM in tapping mode for the surface topography studies. Figure 2.3 shows the AFM topography of an as-received LAO(001) crystal surface. Note that the surface of the as-received LAO(001) substrate is rough and we cannot see step-terrace structures. Figures 2.3(b)-(d) show that systematic changes occur during the thermal treatment process. Here, the as-received LAO(001) substrates were annealed at 1,000 °C, 1,100 °C, and 1,200 °C for 3 hours in oxygen flow. As the substrate annealing temperature increases, the surface atoms rearrange through diffusion, leading to the formation of sharp step edges over time. In general, the surface smoothness improved, and eventually a well-ordered step-terrace structure formed at 1,200 °C. These experiments show that high-temperature thermal annealing is useful for forming an atomically flat step-terrace structure on an LAO(001) surface.

To examine the detailed surface termination state in the annealed LAO(001) substrates, we performed AFM phase-imaging analysis. Figures 2.3(e)-(h) show the AFM phase images, which were taken simultaneously with the AFM topography images in the same substrate area. In the AFM phase images, a subtle change in the phase angle can arise from variation in the chemical composition on the surface of the specimen [19]. Using the phase contrast, we can observe spatial differences in the surface termination of an LAO(001) substrate [20, 21]. For the as-received LAO(001) substrate surface with a mixed termination (i.e., LaO and AlO₂ layers), the spatial distribution of the phase

contrast is highly inhomogeneous. The step-edge and terrace regions exhibit different colors of bright and dark brown in the phase image, respectively. After annealing at 1,000 °C, the phase contrast decreases significantly, and the AFM phase image becomes more uniform, with little color contrast. On the other hand, after annealing at 1,100 °C or higher temperature, the AFM phase images show a distinct contrast.

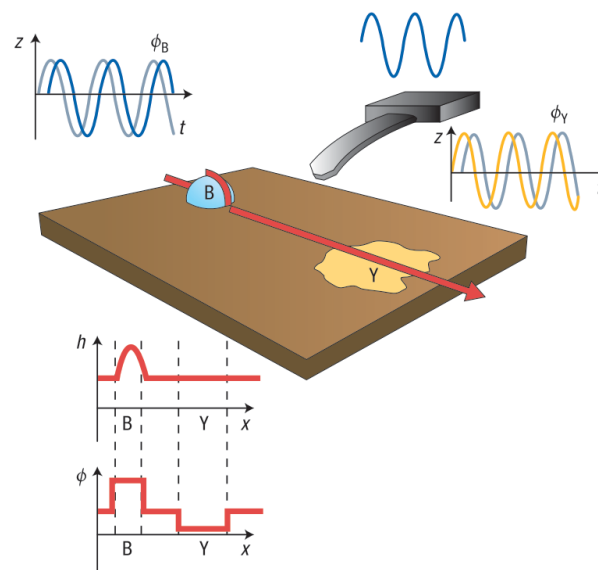


Figure 2.2 Schematic description of tapping mode atomic force microscopy with a constant amplitude. In addition to the height (h), phase-shift signal (Φ) is obtained. The phase-shift depends on the dissipated energy on the sample surface, and can be used to detect local compositional change. Adapted from [19].

Line profiles of AFM images provide further insight into the evolution of surface termination with annealing temperature. Figure 2.3(i) shows both topographic and phase line profiles of LAO after thermal annealing at 1,000 °C. Note that there is a peak-to-valley height variation of about 0.4 nm (the blue line) and only slight phase variations (the red line). This indicates that the 1,000 °C-annealed LAO(001) has a singly terminated surface within the resolution of AFM imaging. This result is consistent with earlier reports of AlO₂-terminated LAO(001) substrate surfaces via thermal annealing [22, 23]. However, as shown in Fig. 2.3(b), there is strong meandering along the step edges and many holes in the terraces probably due to the low surface diffusion rate. This indicates that an atomically flat LAO(001) surface with straight step edges cannot be obtained after 1,000 °C annealing.

Moreover, we cannot obtain a singly terminated surface of the LAO(001) substrate by increasing the annealing temperature to 1,200 °C. Figure 2.3(j) shows the topographic [phase] profiles for the 1,200 °C-annealed sample along the lines marked in Fig. 2.3(d) [Fig. 2.3(h)]. Although well-arranged step-terrace-like features are visible in Fig. 2.3(d), both the height and phase signals are spatially inhomogeneous within each terrace. Note that the peak-to-valley height difference corresponds to half a unit cell. The LaO and AlO₂ sub-layers are alternately stacked in LAO(001) and the presence of half-unit-cell height differences demonstrates that the surface termination in the bright and dark regions must be different. It is probable that surface reconstruction, cation segregation, or the intermixing of La and Al atoms near the surface occur, driven by the entropy [16, 24]. This would lead to a non-uniform surface termination. Unlike the as-

received substrate, the segregation of the two different surface terminations is in the scale of several hundred nanometers. This surface evolution after high-temperature annealing was constantly observed irrespective of the pretreatment method (e.g., acid etching), which is consistent with the earlier study [16]. Hence, using thermal treatment as the final procedure is not sufficient for obtaining an atomically flat and singly terminated LAO(001) surface.

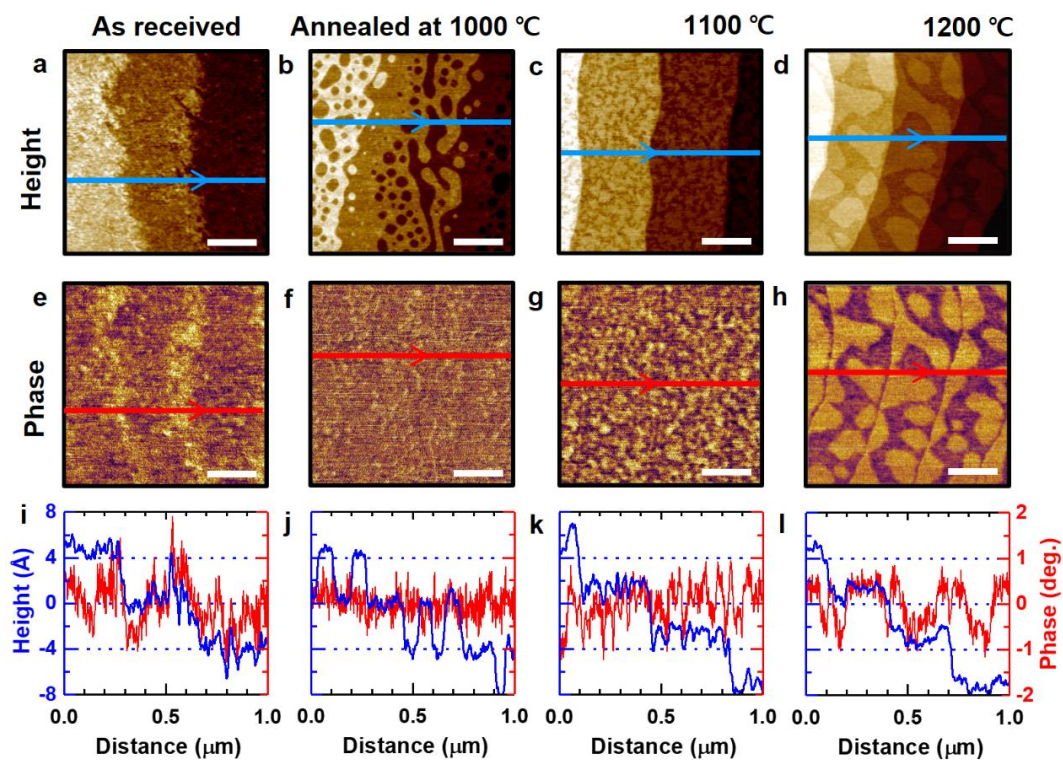


Figure 2.3 Surface topography evolution of single crystal LaAlO_3 (001) [LAO(001)] under various thermal annealing conditions. Atomic Force Microscopy (AFM) height [phase] images measured from (a) [(e)] as-received LAO(001), LAO(001) after annealing at (b) [(f)] 1,000 °C, (c) [(g)] 1,100 °C, (d) [(h)] 1,200 °C for 3 h in oxygen flow. The white scale bars in (a)-(h) are 250 nm long. All images have dimensions $1 \mu\text{m} \times 1 \mu\text{m}$. (i)-(l) Line profiles of the height and phase along, respectively, the blue and red lines in (a)-(d) and (e)-(h).

2.1.4 Chemical etching

In order to achieve an ideal LAO(001) surface for film growth, we developed a new substrate preparation method. We reversed the conventional substrate preparation method consisting of chemical treatment and following post-annealing. Namely, we start with pre-annealing LAO(001) at 1,200 °C to construct a step-terrace structure on an LAO(001) substrate surface. We then use a deionized water leaching process to obtain a single surface termination. Deionized water leaching has already been shown to be effective in controlling the surface termination of perovskite oxides such as SrTiO₃ (001) [25] and BaSnO₃ (001) [26]. During the water leaching process, water-soluble La(OH)₃ may be created on the LAO(001) surface [27]. It is possible that the deionized water only acts as an etchant for the La(OH)₃.

The t_w -dependent evolution of the surface morphology during the water leaching process was found to be rather complicated. Figure 2.4 shows the AFM images taken after the water leaching process for each t_w . Note that all topography images display a well-defined step-terrace structure produced by the pre-annealing process. The annealed LAO(001) substrate ($t_w = 0$ min) in the AFM topography image in Fig. 2.4(a) exhibits a step-terrace structure, but a color contrast emerges in its phase image [inset of Fig. 2.4(a)]. The line profiles of the height and phase responses [Fig. 2.4(e)] clearly show a half-unit-cell height difference and non-zero phase differences, respectively, as discussed earlier. Surprisingly, as shown in Figs. 2.4(b) and 2.4(f), a short treatment ($t_w = 1$ min) with deionized water produces an atomically flat surface with a step-terrace structure.

However, as shown later, this surface is not suitable for practical film growth due to the poor stability in high temperature and moisture. As shown in Fig. 2.4(i), further deionized water treatment ($t_w > 1$ min) makes the surface rougher at first but smoother at the end ($t_w > 120$ min). For example, Figs. 2.4(c) and 2(g) show that after water leaching for 60 minutes, the LAO(001) surface is very rough with a mixed termination. When t_w is longer than 120 minutes, we can obtain a very smooth LAO(001) substrate again. As shown in Fig. 2.4(d), the step-terrace morphology of the water-leached LAO(001) substrate ($t_w = 120$ min) is very sharp and there is no phase contrast [inset of Fig. 2.4(d)]. In the corresponding height and phase profiles [Fig. 2.4(h)], steps are one-unit-cell high and the phase signals show no contrast. For even longer $t_w > 120$ min, the surface termination and roughness do not show notable changes. The t_w -dependent evolution in Fig. 2.4 implies that we can obtain a stable and singly terminated LAO(001) surface with pre-annealing at 1,200 °C and following deionized water treatments for longer than 2 hours.

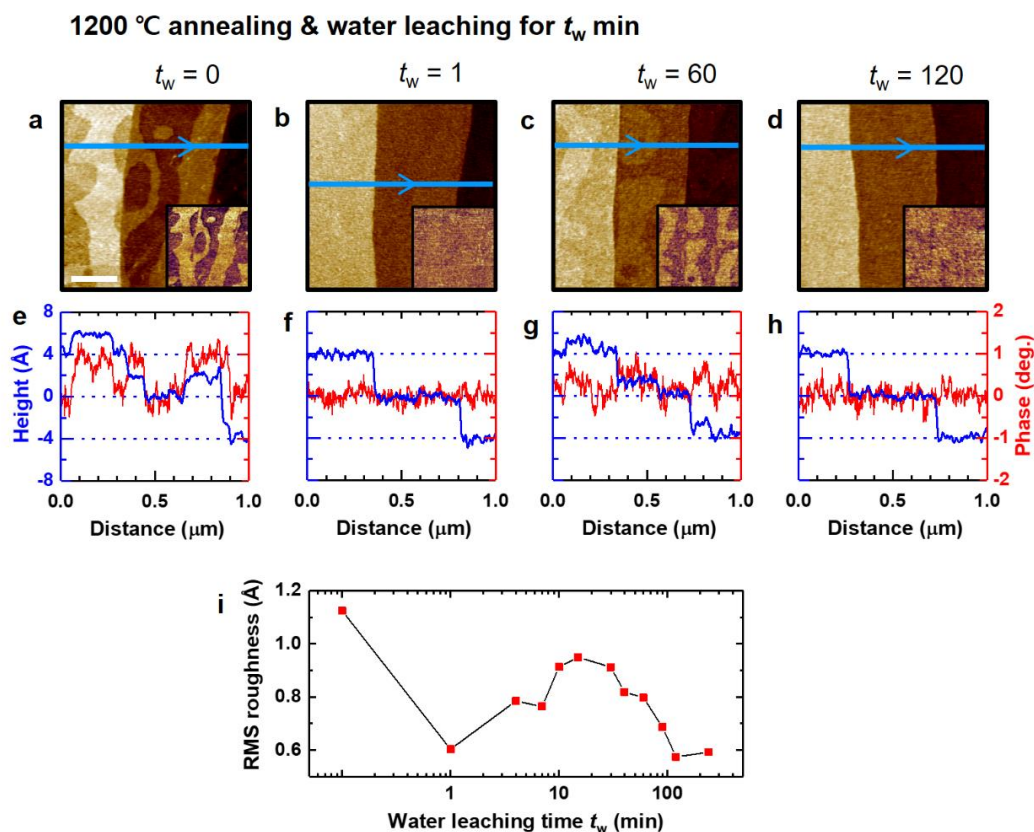


Figure 2.4 Surface topography evolution of annealed LAO(001) surfaces during deionized water leaching. (a)–(d) AFM height images of annealed (1,200 °C for 3 h in oxygen flow) LAO(001) single crystal after ultrasonic agitation in deionized water for leaching times (t_w) = 0, 1, 60, and 120 min. The white scale bars in (a) is 250 nm long. All images have dimensions 1 $\mu\text{m} \times 1 \mu\text{m}$. The inset in (a)–(d) shows the corresponding phase images. (e)–(h) Line profile of height and phase along the blue lines in (a)–(d). (i) t_w -dependent surface roughness of LAO(001) surfaces.

2.1.5 Surface termination analysis by ion scattering spectroscopy

We performed CAICISS analysis to determine quantitatively the chemical compositions of the terminating layers in the water-leached LAO(001) surfaces [29]. As shown in Fig. 2.5(a), when the He ion beam is aligned along the [111] direction of the LAO(001) substrate, only the cations of the topmost atomic layer can cause backscattering [30]. All the other cations in deeper layers are hidden due to the shadowing effect. Figure 2.5(b) shows the time-of-flight (TOF) spectra of scattered He ions, taken along the [111] crystal direction. The TOF spectra contain distinct scattering peaks for He collisions from La, Al, O, and C atoms at the LAO(001) surface. In addition to the signals from the directly backscattered He, there is a broad background associated with multiple scattering events. The backscattering peak intensities were obtained by Gaussian profile fitting (shown in blue, cyan) combined with a smoothly varying polynomial fitted to multiple scattering & background (shown in gray). The scattering peaks of lighter atoms tend to spread to longer flight times. We used two Gaussians (shown in red) for the oxygen peak fitting to account for the asymmetric peak shape. Since we focus on cations (La, Al), this oxygen peak fitting doesn't influence our analysis. The peak area was normalized by the theoretical scattering cross-section for each element, which is approximately proportional to the square of the scattered atomic mass. The surface termination can then be analyzed by looking at La : Al scattering intensity ratio.

As shown in Fig. 2.5(b), the CAICISS peak intensities exhibit dramatic changes with t_w . In the case of the high-temperature-annealed but non-leached substrate ($t_w = 0$

min), the plot in Fig. 2.5(b) appears to show a large La scattering peak seemingly with a La : Al = 7 : 1 peak area ratio. Since the peak areas need to be normalized by scattering cross sections, normalized La : Al ratio is 1 : 4. Assuming a perfect perovskite structure, about 20 % of the surface appears to be terminated by the LaO layer and the rest area is terminated by AlO₂ layer. Note that this ratio may have some uncertainty due to the small intensity of Al peak. Still, it does qualitatively confirm that a considerable amount of La is present on the surface. The La intensity dramatically decreases after the deionized water leaching process, while the Al peak intensity nearly triples for the $t_w = 120$ min sample. Normalized La : Al ratio is approximately 1 : 26 for $t_w = 1$ min and 1 : 105 for the $t_w = 120$ min samples. We can thus conclude that the area of LaO-terminated regions significantly decreases during the water leaching, and the $t_w = 120$ min sample has a singly terminated AlO₂ surface. This result is consistent with the rapid dissolution of LaO species in water.

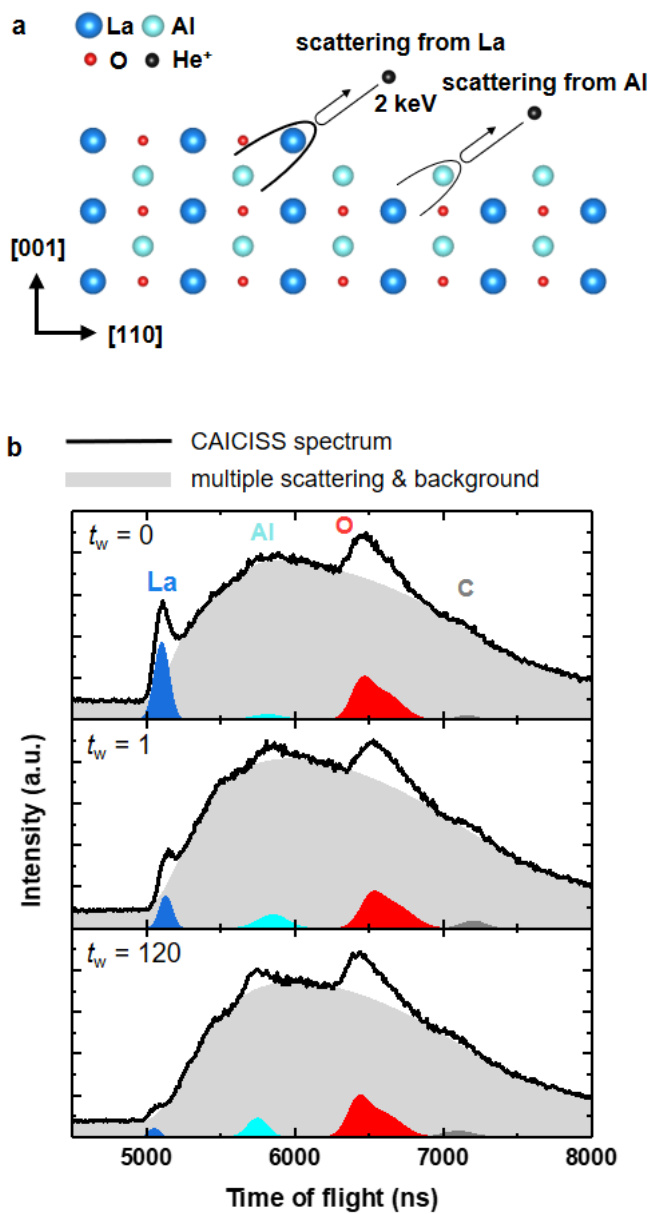


Figure 2.5 Co-axial impact collision ion scattering spectroscopy (CAICISS) analysis on LAO(001) surfaces. (a) Schematic illustration of CAICISS setup. (b) CAICISS spectrum of LAO(001) surfaces with $t_w = 0, 1, \text{ and } 120$ with the fitted peaks of La, Al, O, and C.

2.1.6 Possible surface structures of LaAlO_3 (001) substrates after water leaching

The nearly ideal AlO_2 surface termination achieved in this study might be serendipitous. Note that a polar AlO_2^- surface without charge screening should be energetically unstable due to a polar catastrophe arising from the surface potential. A mixed termination state would, therefore, be energetically preferred on the LAO(001) surface and is indeed observed in the cases of the crystals annealed at high temperature. Recently, it was theoretically predicted that the negative polarity of the surface AlO_2^- layer can be compensated for by hydration or the formation of oxygen vacancies, which can stabilize uniform AlO_2 termination on LAO(001) surfaces [31]. Considering the fact that hydrated $\text{Al}(\text{OH})_3$ is slightly soluble in water [32], an AlO_2 -terminated LAO(001) surface would not be sustainable in the water leaching process. Hence, it is more plausible that the AlO_2 surface termination layer in the LAO(001) substrate might be oxygen-deficient, that is, AlO_{2-x} . However, determination of the oxygen vacancy density in the surface layer is quite difficult for any oxide material. Further investigations are highly desirable to determine the actual stoichiometry of the topmost atomic layer.

It is notable that a seemingly singly terminated surface appears in the intermediate stage of the water leaching process ($t_w = 1$ min). The AFM topography and phase images [Fig. 2.4(b)] suggests that the intriguing surface might be atomically flat with one-unit-cell high steps. Namely, it is actually similar to the single homogeneous layer case with a nearly zero phase contrast. However, this surface morphology is not

stable during the further water leaching. We also tested the surface stability of the $t_w = 1$ min sample during further reannealing and compared it with the case of the $t_w = 120$ min sample. The samples were annealed again at 700 °C in a high vacuum (an oxygen partial pressure of 10^{-6} Torr) for 1 hour. We found that the $t_w = 1$ min sample surface cannot remain atomically flat and singly terminated, while the $t_w = 120$ min sample surface remains intact [28]. Furthermore, as shown in Fig. 2.4(c), the uniform termination of the $t_w = 1$ min surface degrades over several tens of minutes of continuous water leaching treatments. Some regions with height differences of half a unit cell reappear, leading to a mixed termination state on the LAO(001) surface. Therefore, the $t_w = 1$ min LAO(001) substrate is not suitable for the practical growth of complex oxide films and heterostructures.

The CAICISS experiments also indicated that the $t_w = 1$ min LAO(001) surface has incomprehensive stoichiometry. They showed that the La : Al ratio is about 1 : 26, which means that the surface is Al-rich. Based on the polar-angle-dependent CAICISS measurements discussed in the Supplemental Material, the crystallinity of the topmost unit cell layer appears to be low [28]. Possible mechanisms that can explain the AFM and CAICISS results include the presence of a particular surface reconstruction or, more likely, a layer with either La vacancy defects or La-Al antisite substitutions [24]. Further studies are required to understand the atomic-scale origin of this intermediate surface. The incomprehensive stoichiometry also makes it difficult to use the $t_w = 1$ min LAO(001) substrate for practical oxide thin film growth.

2.1.7 Fabrication of an abrupt oxide heterointerface on LaAlO_3 (001) surfaces

The real impetus of our studies is to secure a method to grow atomically sharp heterointerfaces with the AlO_2 -terminated LAO(001). We corroborated the availability of the AlO_2 -terminated LAO(001) substrate for the growth of oxide thin films. Here we grew a prototypical SRO film via PLD on the AlO_2 -terminated LAO(001) substrate prepared by water leaching. We investigated the atomic termination sequence of the SRO/LAO(001) heterointerface with the STEM. As shown in Fig. 2.6(a), the HAADF image confirmed the atomically sharp SRO/LAO interface. To determine the stacking sequence at the interface, we plotted the intensity profile integrated along the yellow dashed box. The peak intensities of atoms (Sr, Ru, La, and Al) are determined by the atomic number. As shown in Fig. 2.6(b), the profile signifies an interfacial stacking sequence of RuO_2 - SrO - AlO_2 - LaO . This demonstrates that the AlO_2 -terminated LAO(001) prepared by water leaching is highly stable even in the usual deposition environment of complex oxide thin films. The physical adsorbates (e.g., water molecules, carbonates) that may occur during the water leaching process appear to be effectively removed by the high-temperature deposition environment. Therefore, this substrate preparation method can be applicable for realizing atomically sharp heterointerfaces on LAO(001) substrates.

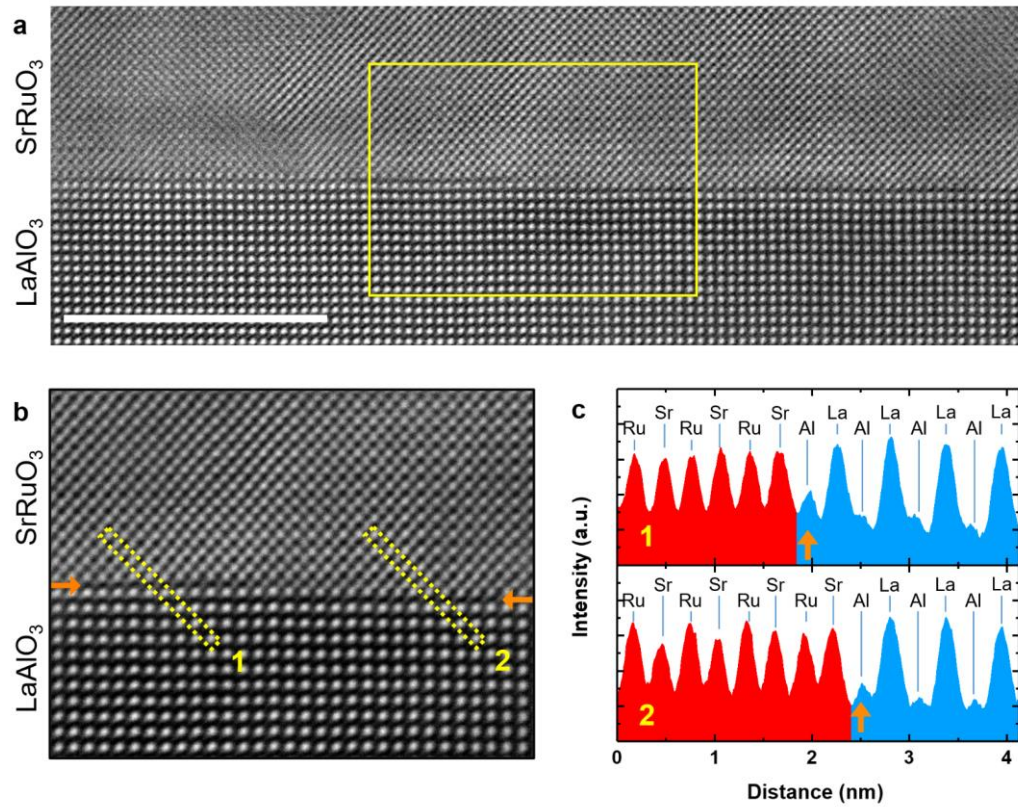


Figure 2.6 Cross-sectional scanning transmission electron microscopy (STEM) analysis on SrRuO₃/LaAlO₃ (001) interfaces. (a) High angle annular dark field (HAADF) STEM image with the zone axis along the [100]-orientation of LaAlO₃. (a) HAADF-STEM analysis on the yellow box in (a). (c) Line profiles of STEM intensity along the yellow dashed boxes in (b).

2.1.8 Other substrates

In this thesis, we used a variety of perovskite oxide substrates to fabricate complex oxide heterostructures. As in the case of the LaAlO₃ (001), the preparation methods consist of surface crystallization by thermal annealing, and selective chemical etching if necessary. As examples, the atomically flat and singly terminated surfaces of LaAlO₃ (001), SrTiO₃ (001), LSAT (001), and GdScO₃ (110) is shown in Fig. 2.7.

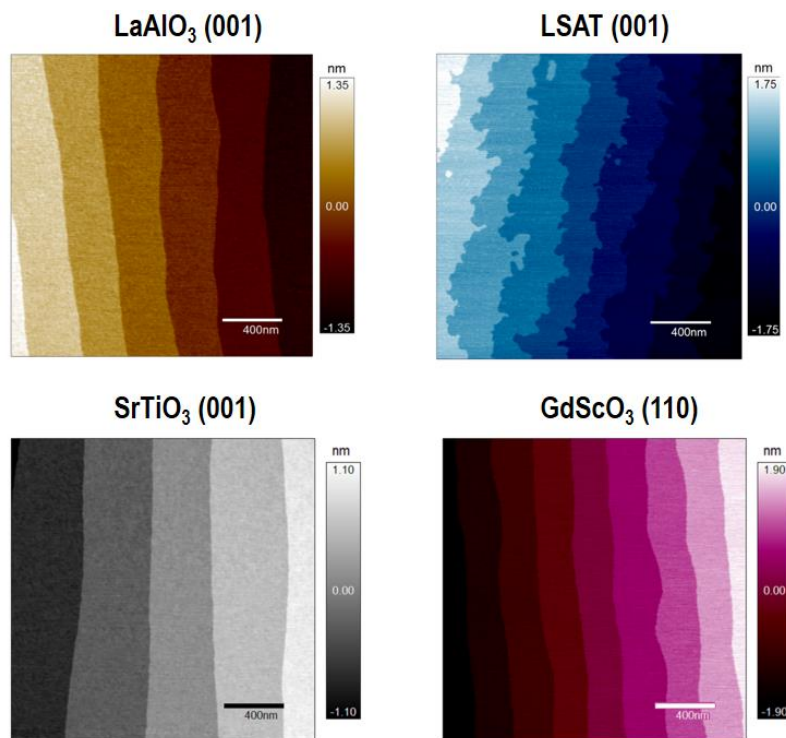


Figure 2.7 Atomically flat and singly terminated surfaces of LaAlO₃ (001), LSAT (001), SrTiO₃ (001), and GdScO₃ (110).

2.2 Pulsed laser deposition of epitaxial oxide heterostructures

2.2.1 Pulsed laser deposition

Pulsed laser deposition (PLD) is a physical vapor deposition technique for thin film growth [33,34]. The PLD of thin film is schematically shown in Fig. 2.8. It is conducted inside ultra-high vacuum chamber with appropriate gas environments (O_2 , O_3 , Ar, H_2 , and so on). In the process, a high-energy pulsed laser is focused on a target of the material that is to be deposited. The focused laser ablates the target, creates a plasma plume, and finally transfers the materials to a substrate. Proper control of the substrate temperature and background gas allows the growth of the thin film.

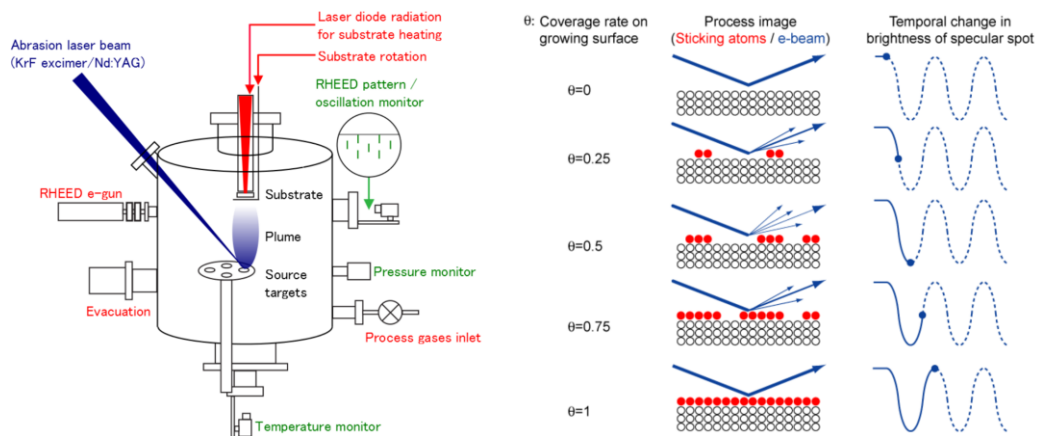


Figure 2.8 Schematic description of pulsed laser deposition and atomic-scale control of epitaxy. Adapted from [<http://www.pascal-co-ltd.co.jp>].

The growth process of the PLD can be monitored and controlled through reflection high-energy electron diffraction (RHEED) technique [35]. In RHEED, a high-energy (10 – 30 keV) electron beam is focused onto the surfaces of the substrate/film with a small incidence angle (0.1 – 5°). Due to the small incidence angle, the RHEED can interact with only the few topmost layers, and do not disturb the ablated plasma plume. The incident electrons diffract from atoms at the surface of the substrate/film and form a diffraction pattern, which can be detected in photo-luminescent screen installed at the opposite side of the PLD chamber. The RHEED pattern provides information of crystal structure and morphology of the surfaces. Monitoring the RHEED intensity allows the real-time control of the growth in unit-cell scale. Figure 2.8 illustrates the RHEED monitoring process. During the growth of a film, the RHEED intensity reflects the completeness of the layer being deposited, as it depends on the kinds of atoms and surface roughness. In layer-by-layer growth, the RHEED intensity shows oscillatory behavior, and one oscillation corresponds to the growth of monolayer. Equipped with the RHEED, the PLD can carry out atomic-scale control of epitaxy.

From many perspectives, the PLD is particularly useful technique for constructing complex oxide heterostructures and superlattices. A KrF excimer laser with a wavelength of 248 nm (5 eV) is commonly used for the PLD and can ablate most oxides whose band gap is usually lower than the photon energy. The highly kinetic plume can reach the substrate even at the high background gas pressure of up to 1 Torr. By using the wide range of background oxygen partial pressure, the PLD can effectively control the oxygen stoichiometry of the deposited oxide films. The nearly stoichiometric transfer of

the target materials to the substrate makes the PLD suitable for growing multi-component complex oxides. In addition, thin films can be deposited with only the preparation of additional targets, providing excellent accessibility to the growth of various materials. Combining these features, the PLD offers a fast and versatile fabrication of epitaxial oxide heterostructures in which a wide range of properties are integrated with atomic-scale precision.

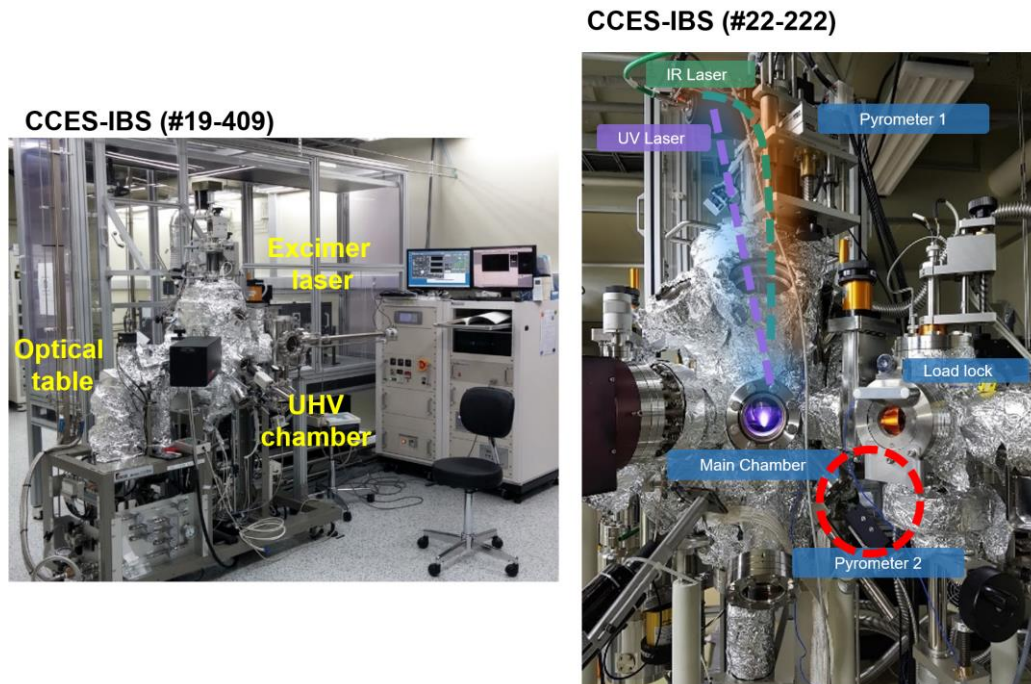


Figure 2.9 Pulsed laser deposition systems in use.

2.2.2 Parameters of pulsed laser deposition

The most important factor in the optimization of ABO_3 perovskite oxide thin films is the stoichiometry ($A : B : O = 1 : 1 : 3$). In general, the oxygen stoichiometry is controlled by the background gas pressure, and A/B ratio is optimized by adjusting a variety of the PLD parameters such as substrate temperature, background gas pressure, laser fluence, laser repetition rate, laser spot size, target-to-substrate distance, composition of target, and so on. In this chapter, the first three major PLD parameters are discussed.

The substrate temperature determines the cation stoichiometry, thermodynamic stability, crystallinity, and growth mode. First, when the constituting A or B cation is volatile, as in case of $SrRuO_3$ and $SrIrO_3$, increasing the substrate temperature evaporates the volatile species [36,37]. If the substrate temperature is properly optimized, a self-regulated growth can be realized, which is not possible if both A and B cations are non-volatile. Second, the higher the substrate temperature, the faster the film transits to the most stable state. For the given composition of the film, the high substrate temperature results in a ground state of the film and the enhanced crystallinity. Rather than the conventional layer-by-layer growth mode, step-flow growth (stable surface) and three-dimensional growth (unstable surface) is preferred at the high temperature.

The background gas pressure determines the cation stoichiometry, oxidation state. First, A and B cations have different masses and ionic radius, and accordingly different scattering cross-section with the background gas molecules. Background gas

pressure often selectively scatter the cation and induces non-stoichiometry during the PLD process. Second, the oxidation states of film are most directly dependent on the background gas pressure. Multiple oxidation states are unique and functional properties of the transition metal oxides. Precise control of the background gas pressure can stabilize the target oxidation states. In extreme cases, the abnormal Co^{4+} and Mo^{4+} states have been stabilized as perovskite oxide films using the ozone (O_3) and hydrogen ($\text{Ar} + \text{H}_2$) atmospheres, respectively [38,39].

The laser fluence determines the cation stoichiometry and formation of defects. First, although the detailed mechanism is not clear, the cation stoichiometry is highly dependent on the laser fluence in almost all known PLDs of ABO_3 film [40]. Second, the high laser fluence increases the kinetic energy of the plasma plume and the defect density of the resulting films [41]. The defect formation can also be mediated by increasing the background gas pressure. The increased scattering of the background gas can reduce the kinetic energy of the plume. The laser fluence is particularly important in the sense that it allows selective control of the aforementioned factors without altering thermodynamic property and oxidation state of the film.

2.2.3 Optimization of high-quality perovskite oxide thin films

A complicated growth mechanism of the PLD require careful control of each growth parameters. Each of the parameter can seriously affect the stoichiometry of films and their physical properties. Lattice parameter is a good indicator for the stoichiometry

and the quality of the thin films. Stoichiometric films usually have a locally extremum of the lattice parameter. The growth optimization of perovskite titanates is shown in Fig. 2.10. At fixed substrate temperature and background gas pressure, we systematically varied the laser fluence to grow several $\text{CaTiO}_3/\text{LSAT}$ (001), $\text{SrTiO}_3/\text{SrTiO}_3$ (001), and $\text{BaTiO}_3/\text{GdScO}_3$ (110) thin films. The stoichiometric CaTiO_3 and SrTiO_3 tends to have minimum c-axis lattice constants, while the stoichiometric BaTiO_3 has the maximum. Similar trends have been reproduced by molecular beam epitaxy of perovskite titanates films [42-44].

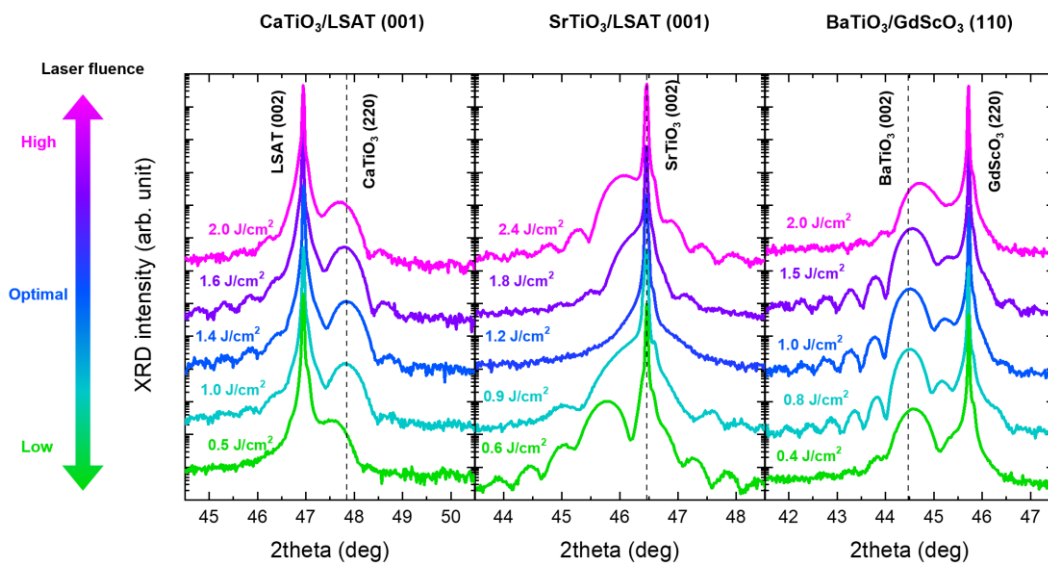


Figure 2.10 Optimization of the PLD of perovskite titanates by varying laser fluence

2.3 Summary

In summary, we realized atomically flat, singly terminated surfaces of perovskite oxide substrates via thermal annealing and chemical etching. On the well-defined substrate surfaces, we grow epitaxial oxide thin films using pulsed laser deposition. The cation stoichiometry of the films was carefully optimized by varying the PLD parameters. The methods described in this chapter would realize high-quality epitaxial oxide heterostructures and facilitates the exploration of exotic phenomena at complex oxide heterointerfaces. Throughout this dissertation, we prepare epitaxial oxide heterostructures using the methods.

References

- [1] H. Y. Hwang, *et al.*, Nat. Mater. **11**, 103 (2012).
- [2] P. Zubko, S. Gariglio, M. Gabay, P. Ghosez, and J.-M. Triscone, Annu. Rev. Condens. Matter Phys. **2**, 141 (2011).
- [3] A. Ohtomo and H. Y. Hwang, Nature **427**, 423 (2004).
- [4] D. P. Kumah, *et al.*, Phys. Rev. Appl. **2**, 054004 (2014).
- [5] P. Yu, *et al.*, Proc. Natl. Acad. Sci. **109**, 9710 (2012).
- [6] Y. J. Shin, *et al.*, Adv. Mater. **29**, 1602795 (2017).
- [7] L. Wang, *et al.*, Adv. Mater. **29**, 1702001 (2017).
- [8] T. Yajima, Y. Hikita, and H. Y. Hwang, Nat. Mater. **10**, 198 (2011).
- [9] M. Kawasaki, T. Maeda, R. Tsuchiya, and H. Koinuma, Science **266**, 1540 (1993).
- [10] A. Biswas, C.-H. Yang, R. Ramesh, and Y. H. Jeong, Prof. Surf. Sci. **92**, 117 (2017).
- [11] M. Lippmaa, *et al.*, Appl. Surf. Sci. **130**, 582 (1998).
- [12] D. G. Schlom, *et al.*, Annu. Rev. Mater. Res. **37**, 589 (2007).
- [13] D. Sando, A. Barthélémy, and M. Bibes, J. Phys. Condens. Matter **26**, 473201 (2014).
- [14] M. Minohara, *et al.*, Nano. Lett. **14**, 6743 (2014).
- [15] T. Higuchi, Y. Hotta, T. Susaki, A. Fujimori, and H. Y. Hwang, Phys. Rev. B **79**, 075415 (2009).
- [16] A. J. H. van der Torren, S. J. van der Molen, and J. Aarts, Phys. Rev. B **91**, 245426 (2015).
- [17] C. H. Lanier, *et al.*, Phys. Rev. Lett. **98**, 086102 (2007).

-
- [18] M. Yoshimoto, *et al.*, Appl. Phys. Lett. **65**, 3197 (1994).
- [19] R. Garca, R. Magerle, and R. Perez, Nat. Mater. **6**, 405 (2007).
- [20] R. Bachelet, F. Sanchez, F. J. Palomares, C. Ocal, and J. Fontcuberta, Appl. Phys. Lett. **95**, 141915 (2009).
- [21] R. Gunnarsson, A. S. Kalabukhov, and D. Winkler, Surf. Sci. **603**, 151 (2009).
- [22] D.-W. Kim, *et al.*, Appl. Phys. Lett. **74**, 2176 (1999).
- [23] Z. Q. Liu, *et al.*, AIP Adv. **2**, 012147 (2012).
- [24] X. Luo, B. Wang, and Y. Zheng, Phys. Rev. B **80**, 104115 (2009).
- [25] J. G. Connell, B. J. Isaac, G. B. Ekanayake, D. R. Strachan, and S. S. A. Seo, Appl. Phys. Lett. **101**, 251607 (2012).
- [26] W.-J. Lee, *et al.*, Appl. Phys. Lett. **111**, 231604 (2017).
- [27] D. R. Lide, *CRC Handbook of Chemistry and Physics* (CRC, 2004).
- [28] J. R. Kim, *et al.*, Phys. Rev. Mater. **3**, 023801 (2019).
- [29] M. Katayama, E. Nomura, N. Kanekawa, H. Soejima, and M. Aono, Nucl. Instrum. Methods Phys. Res. B **33**, 857 (1988).
- [30] T. Ohnishi, *et al.*, Appl. Phys. Lett. **74**, 2531 (1999).
- [31] K. Krishnaswamy, C. E. Dreyer, A. Janotti, and C. G. Van de Walle, Phys. Rev. B **90**, 235436 (2014).
- [32] K. H. Gayer, L. C. Thompson, and O. T. Zajicek, Can. J. Chem **36** (9), 1268 (1958).
- [33] D. G. Chrisey and G. K. Hübner, *Pulsed Laser Deposition of Thin Films* (John Wiley & Sons, 1994).
- [34] R. Eason, *Pulsed laser deposition of thin films: applications-led growth of functional*

materials (John Wiley & Sons, 2007).

[35] A. Ichimiya, P. I. Cohen, *Reflection high-energy electron diffraction* (Cambridge University Press, 2004).

[36] T. Ohnishi and K. Takada, *Appl. Phys. Express* **4**, 025501 (2011).

[37] K. Nishio, H. Y. Hwang, and Y. Hikita, *APL Mater.* **4**, 036102 (2016).

[38] H. Jeen, *et al.*, *Nat. Mater.* **12**, 1057 (2013).

[39] A. Radetinac, K. S. Takahashi, L. Alff, M. Kawasaki, and Y. Tokura, *Appl. Phys. Express* **3**, 073003 (2010).

[40] T. Ohnishi, K. Shibuya, T. Yamamoto, and M. Lippmaa, *J. Appl. Phys.* **103**, 103703 (2008).

[41] A. R. Damodaran, E. Breckenfeld, Z. Chen, S. Lee, and L. W. Martin, *Adv. Mater.* **26**, 6341 (2014).

[42] C. M. Brooks, *et al.*, *Appl. Phys. Lett.* **94**, 162905 (2009).

[43] R. C. Haislmaier, *et al.*, *Adv. Funct. Mater.* **26**, 7271 (2016).

[44] Y. Matsubara, K. S. Takahashi, Y. Tokura, and M. Kawasaki, *Appl. Phys. Express* **7**, 125502 (2014).

Chapter 3

Stabilizing hidden room-temperature ferroelectricity via a metastable atomic distortion pattern

Nonequilibrium atomic structures can host exotic and technologically relevant properties in otherwise conventional materials. Oxygen octahedral rotation (OOR) forms a fundamental atomic distortion in perovskite oxides, but only a few OOR patterns are predominantly present at equilibrium. This has restricted the range of possible properties and functions of perovskite oxides, necessitating the utilization of nonequilibrium OOR patterns. Here, we report that a designed metastable OOR pattern leads to robust room-temperature ferroelectricity in CaTiO_3 , which is otherwise nonpolar down to 0 K. Guided by density functional theory, we selectively stabilize the metastable OOR pattern, distinct from the equilibrium pattern and exceptionally cooperative with ferroelectricity, in heteroepitaxial films of CaTiO_3 . Atomic-scale imaging combined with deep neural network analysis confirms a close correlation between the metastable OOR pattern and ferroelectricity. This work reveals a hidden but functional OOR pattern and opens new avenues for designing novel multifunctional materials.

3.1 Background

3.1.1 Pattern of oxygen octahedral rotation

The octahedra can rotate along each of the three Cartesian axes. For each axis, the OOR can be in-phase or out-of-phase with respect to the neighboring plane of octahedra. The patterns of the OOR have been classified using the Glazer notation [1]. The Glazer notation refers to the OOR along a particular Cartesian axis as $a^{+(-)}$ in which a indicates amount of rotation and $+$ ($-$) indicates in-phase (out-of-phase) rotations. For the case of no rotation, a^0 is used. Figure 3.1 depicts the Glazer notation of the 23 possible OOR pattern.

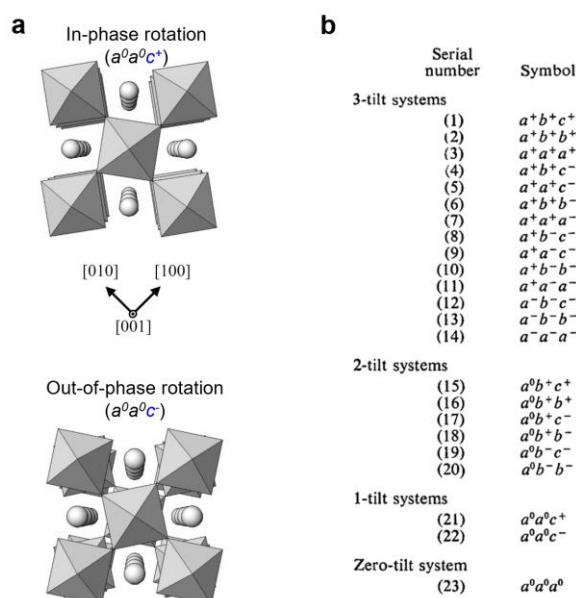


Figure 3.1 (a) Schematic description of in-phase and out-of-phase octahedral rotation. (b) List of possible octahedral rotation pattern. Adapted from [1,2].

Despite the various patterns of the OOR, there has been a serious imbalance in the reported OOR pattern of known materials (Fig. 3.2) [2]. Only 15 OOR patterns have been reported, and they can be divided into three groups listed in Fig. 3.2(b). High-symmetry OOR patterns in group A are found from the perovskites composed of a single A-site cation. When there are multiple A-site cations, the OOR patterns in group B appears. The low-symmetry OOR patterns in group C are observed as intermediates in a phase transition between two of the higher symmetry patterns. It is notable that most perovskite bulks adopt the orthorhombic ($Pnma$) structure, corresponding to the $a^-b^+a^-$ OOR pattern in Glazer notation. Such predominance of the $a^-b^+a^-$ OOR pattern has prevented full structural exploitation of perovskites.

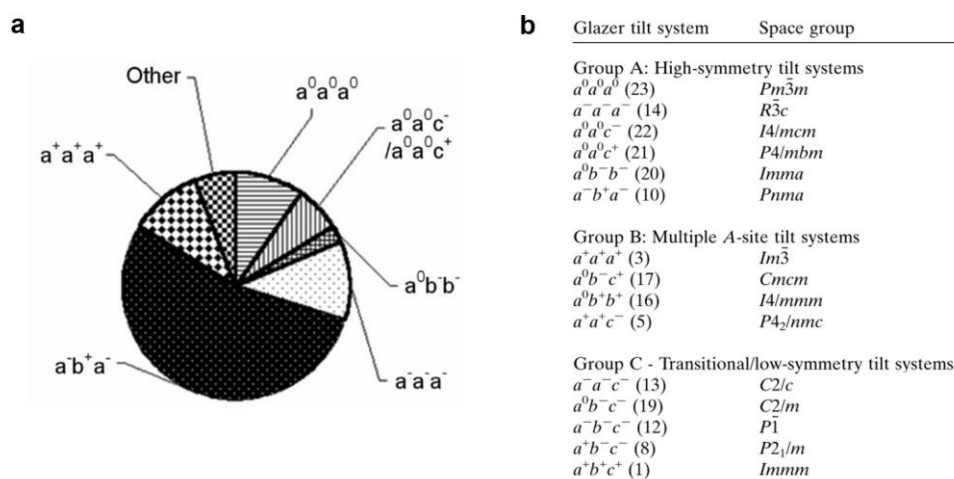


Figure 3.2 (a) Distribution of tilt systems among known perovskites with a single octahedral cation. (b) The 15 tilt systems, space groups of observed structures reported for simple perovskites. Adapted from [2].

3.1.2 Ferroelectricity

Ferroelectricity is a property of materials that have a spontaneous electric polarization that can be reversed by the application of an external electric field [3]. Because of the unique feature, the polarization is dependent on not only the current electric field but also its history, producing a hysteresis loop. It can be used as a non-volatile memory, where up and down polarization may correspond to “0” and “1”. Among perovskite oxides, the first ferroelectricity was discovered in BaTiO₃. In the BaTiO₃, the polarization emerged through the displacements of cations relative to the centrosymmetric position (Fig. 3.3). Then, the discovery of various ferroelectric perovskite oxides including PbTiO₃, KNbO₃, LiNbO₃, and BiFeO₃ followed, and perovskite oxides becomes the most important class of materials in the research on ferroelectricity.

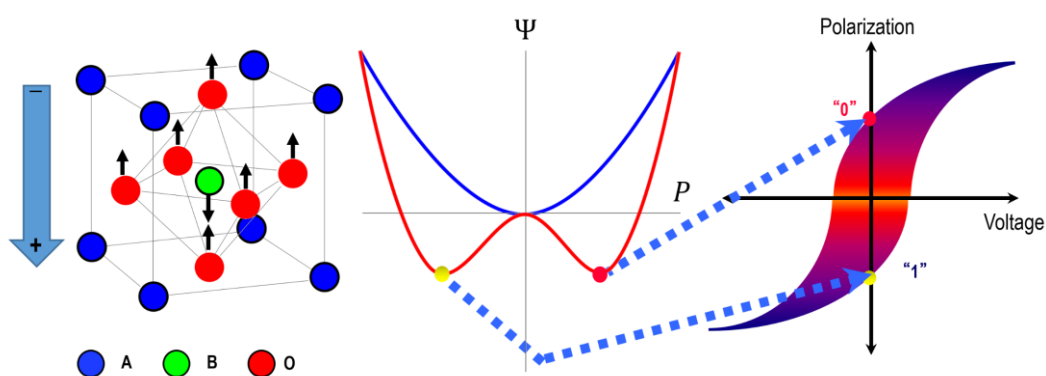


Figure 3.3 Schematic description of ferroelectricity in ABO₃ perovskite oxides. The displacements of cation produce spontaneous and switchable electric polarization.

3.1.3 Structural coupling between OOR and ferroelectricity

The most common $a^-b^+a^-$ OOR pattern has been shown to compete with an important functional property, namely ferroelectricity [4]. The $a^-b^+a^-$ OOR pattern induces A-site antipolar displacements, and it plays a crucial role in suppressing the ferroelectric distortion. As a result, most $Pnma$ perovskites remain paraelectric, even down to 0 K, whereas their cubic phases could have instability for both ferroelectric and OOR distortions. This has motivated recent attempts to utilize nonequilibrium OOR, e.g., via artificial heteroepitaxy [5-7]. Despite extensive works [8-11], however, there is still a lack of studies on engineering the pattern itself of OOR and then generating novel functionalities. Thus, it will be of great interest to design and stabilize a nonequilibrium OOR pattern, distinct from the original $a^-b^+a^-$ pattern and compatible with ferroelectricity.

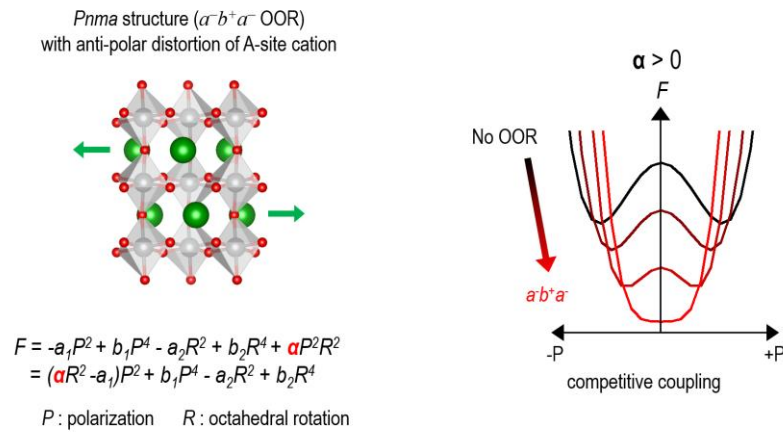


Figure 3.4 Schematic description of competitive coupling between ferroelectricity and OOR in $a^-b^+a^-$ OOR pattern.

In this chapter, we designed a means to stabilize a nonequilibrium OOR pattern of CaTiO_3 in oxide heterostructures. Unlike the original $a^-b^+a^-$ pattern, the metastable OOR pattern appears to be compatible with ferroelectricity, leading to the emergence of room-temperature ferroelectricity. Moreover, we combined transmission electron microscopy techniques with deep neural network analysis and revealed the strong coupling between the metastable OOR pattern and ferroelectricity. Our work suggests that engineering the nonequilibrium OOR pattern unveils the hidden functionalities of materials.

3.2 Experimental methods

3.2.1 Growth and characterization of thin films

Commercially available LaAlO_3 single crystal substrates (Crystec GmbH, Germany) were used. Prior to the growth, LaAlO_3 (111) and (001) substrates were dipped in deionized water and sonicated for 2 hours. Then, the substrates were annealed in the growth chamber *in-situ*. The annealing temperature, background gas pressure, and annealing time were 1,000 °C, $<1.0 \times 10^{-7}$ mTorr of pure oxygen, and 1 hour, respectively. Using this procedure for preparing substrates, we realized clean (111)-oriented heterointerfaces despite the high surface polarity. We observed no structural defects or interfacial disorder over a large area.

CaTiO_3 and LaNiO_3 thin films were grown using PLD. For the growth of thin films, the substrate temperature and background oxygen partial pressure were kept at

600 °C and 10 mTorr, respectively. Polycrystalline $\text{Ca}_{1.1}\text{TiO}_{3.1}$ and LaNiO_3 targets were ablated with a KrF excimer laser (LPXpro, Coherent, USA). The *in-situ* RHEED intensity monitoring shown in Fig. 3.5(a) indicates layer-by-layer growth of CaTiO_3 on the LaAlO_3 (111) substrate. The grown films had smooth surfaces with step and terrace structures [Fig. 3.5(b)].

X-ray diffraction (XRD; AXS D8 with a Vantec line-detector, Bruker, USA) was used for structural analysis of thin films. All films were epitaxially grown on the LaAlO_3 (111) substrates and clear Kiessig fringes are seen [Fig. 3.5(c)]. For ultrathin films with a thickness of several nanometers, we used Huber six-circle diffractometers at Sector 3A of the Pohang Light Source.

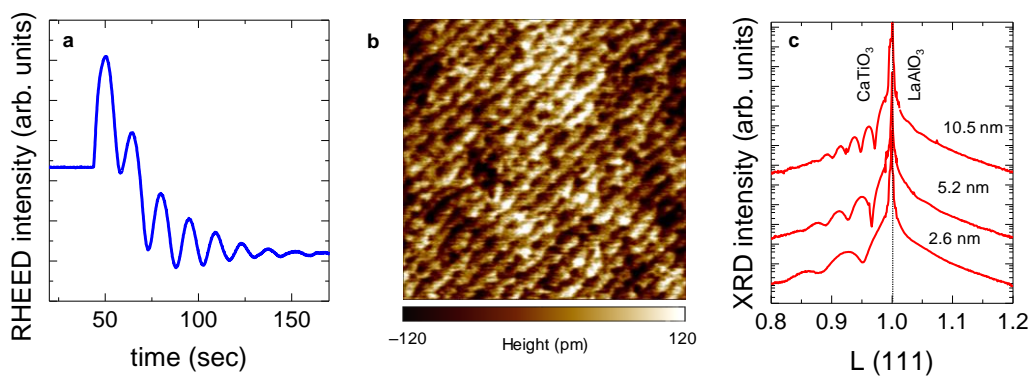


Figure 3.5 Characterization of $\text{CaTiO}_3/\text{LaAlO}_3$ (111) thin films. (a) RHEED intensity monitoring showing layer-by-layer growth of CaTiO_3 thin film on LaAlO_3 (111) substrate. (b) AFM height image of 2.5 nm-thick $\text{CaTiO}_3/\text{LaAlO}_3$ (111) thin film. (c) X-ray diffraction (XRD) data on $\text{CaTiO}_3/\text{LaAlO}_3$ (111) thin films, measured around LaAlO_3 (111) diffraction peaks. CaTiO_3 are epitaxially grown on LaAlO_3 (111) substrates.

3.2.2 Piezoresponse force microscopy (PFM)

Switchable ferroelectric polarization was confirmed using scanning probe microscopy (Cypher, Asylum Research, UK) with conductive probes (PPP-EFM, Nanosensors). Dual AC resonance tracking PFM was used to read/write bi-polar domain patterns and obtain d_{33} values as a function of the applied voltage. To exclude the contribution of electrostatic force to PFM signals, PFM was performed at higher-harmonic resonance frequency near 900 kHz.

3.2.3 Density functional theory calculation

We performed first-principles DFT calculations within the local density approximation (LDA) using the Vienna *ab-initio* simulation package (VASP). The projector augmented wave method was used with an energy cut-off of 500 eV. The Brillouin zone was sampled with an $8 \times 8 \times 8$ k -point grid for the 5-atom unit cell of rhombohedral CaTiO_3 and a $4 \times 4 \times 4$ k -point grid is used for a $2 \times 2 \times 2$ supercell with 40 atoms to accommodate the relevant octahedral rotations and polar distortions. Convergence was reached if the consecutive energy difference is less than 10^{-6} eV. The structural relaxation was conducted with a force threshold of $0.001 \text{ eV \AA}^{-1}$. The polarization was calculated using the Berry-phase method as implemented in VASP. The phonon dispersion was calculated using the density functional perturbation theory implemented in the VASP and phonopy with an increased energy cut-off (600 eV) and convergence threshold (10^{-8} eV).

3.2.4 Second harmonic generation (SHG)

The symmetry of CaTiO_3 thin films grown on (001) and (111) LaAlO_3 substrate was characterized by SHG. Figure 3.6 displays the experimental set-up for the SHG. The 800-nm femtosecond wave, with an 80-MHz repetition rate and 30-fs duration, was irradiated on the thin films with an incidence angle of 45° as a fundamental wave (Vitarat, Coherent). We focused the beam spot size into 1–30 μm . The polarization states of a fundamental and generated second harmonic wave were controlled to be p- or s-polarization by a half-wave plate and polarizer, respectively. To avoid the detection of the fundamental wave, we isolated the second harmonic wave using the short pass and bandpass filters. We monitored the intensity of the second harmonic response using a photomultiplier tube at the end of the optical path.

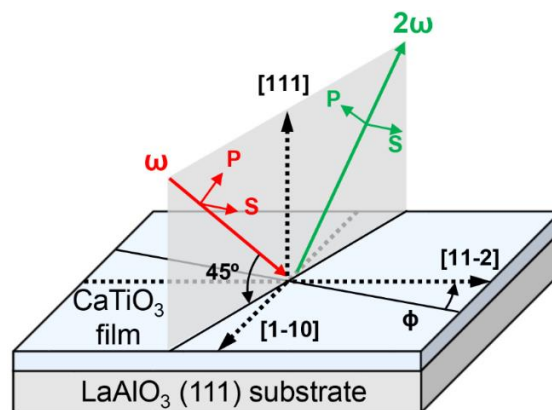


Figure 3.6 Experimental set-up for reflection second harmonic generation. 800-nm femtosecond wave is irradiated on the sample with an incidence angle of 45 degrees. “p” (“s”) indicates parallel (perpendicular) polarization with respect to the plane of incidence.

3.2.5 Scanning transmission electron microscopy (STEM)

Cross-sectional specimens oriented along the $[1\bar{1}0]$ direction of both samples were prepared by conventional mechanical flat polishing with less than 10 μm thickness. Mechanically polished samples were further milled using a 3 keV Ar ion beam for $\text{CaTiO}_3/\text{LaAlO}_3$ (001) and 2 keV for $\text{CaTiO}_3/\text{LaAlO}_3$ (111) and using a 0.1 keV Ar ion beam for removing surface damage from both samples (PIPS II, Gatan, USA). ABF-STEM images for light elements, i.e., oxygen, were acquired using STEM (ARM 200F, JEOL, USA) at 200 kV with a spherical aberration corrector (ASCOR, CEOS GmbH, Germany) for each of the $\text{CaTiO}_3/\text{LaAlO}_3$ (001) and (111) samples with a convergence angle of 27 mrad. Additionally, to minimize the electron beam-induced phase transition of the metastable $\text{CaTiO}_3/\text{LaAlO}_3$ (111) sample, imaging was also conducted at an 80-kV accelerating voltage with a convergence angle of 27 mrad.

3.3 Results and Discussion

3.3.1 Theoretical survey on nonequilibrium octahedral rotation pattern

Taking CaTiO_3 —the first discovered perovskite compound—as a model system, we explore the feasibility of achieving ferroelectricity via its nonequilibrium OOR patterns. Bulk CaTiO_3 has the $Pnma$ space group symmetry and the $a^-b^+a^-$ OOR pattern below 1512

K [12] and exhibits a stable nonpolar, paraelectric phase down to 0 K; bulk CaTiO_3 exhibits antipolar Ca displacements. It is notable that CaTiO_3 is an incipient ferroelectric material with a negative Curie–Weiss temperature [13-15], so that it has potential to be engineered into a ferroelectric phase. Of the 23 possible OOR patterns, we focus on 10 patterns, since the other patterns rarely occur in a single ABO_3 compound [2]. According to our density functional theory (DFT) calculations [Fig. 3.7(c)], the nonpolar $Pnma$ with the $a^-b^+a^-$ OOR pattern has the lowest energy, consistent with the bulk crystal structure of CaTiO_3 . The highest energy is seen in the cubic $Pm\bar{3}m$ without OOR (i.e., $a^0a^0a^0$), which is highly unstable due to the small size of the A-site Ca ion [16]. The other eight OOR patterns are located in between and, to the best of our knowledge, have not been reported in bulk CaTiO_3 . Our theory predicts that among the eight OOR patterns, $a^-a^-a^-$ and $a^+a^+c^-$ allow for polar structures with the space groups $R3c$ and $P4_2/mc$, respectively. Given their moderate energy cost (as small as 100 meV f.u.⁻¹), our DFT calculations indicate the possibility to thermodynamically stabilize the nonequilibrium $a^-a^-a^-$ or $a^+a^+c^-$ pattern and then achieve ferroelectricity in CaTiO_3 .

Here, we take $a^-a^-a^-$ [Fig. 3.8] as the target OOR pattern of CaTiO_3 due to its experimental accessibility, which is discussed later. Our first-principles calculation finds no unstable phonon mode in the polar $R3c$ with the $a^-a^-a^-$ OOR pattern, indicating its metastability [Fig. 3.7(f)]. The calculated polarization value, P , of the $R3c$ CaTiO_3 is 44 $\mu\text{C cm}^{-2}$, and the energy barrier, ΔE , for polarization switching is 16 meV f.u.⁻¹. These values are comparable to those of archetypal ferroelectric perovskites [17], such as BaTiO_3 ($P = 20 \mu\text{C cm}^{-2}$, $\Delta E = 11.6 \text{ meV f.u.}^{-1}$) and PbTiO_3 ($P = 78 \mu\text{C cm}^{-2}$, $\Delta E = 32.6 \text{ meV f.u.}^{-1}$),

whose ferroelectric transition temperatures are 393 and 760 K, respectively. Therefore, artificial stabilization of the metastable $a^-a^-a^-$ OOR pattern may result in robust room-temperature ferroelectricity—hitherto hidden at equilibrium—in CaTiO_3 .

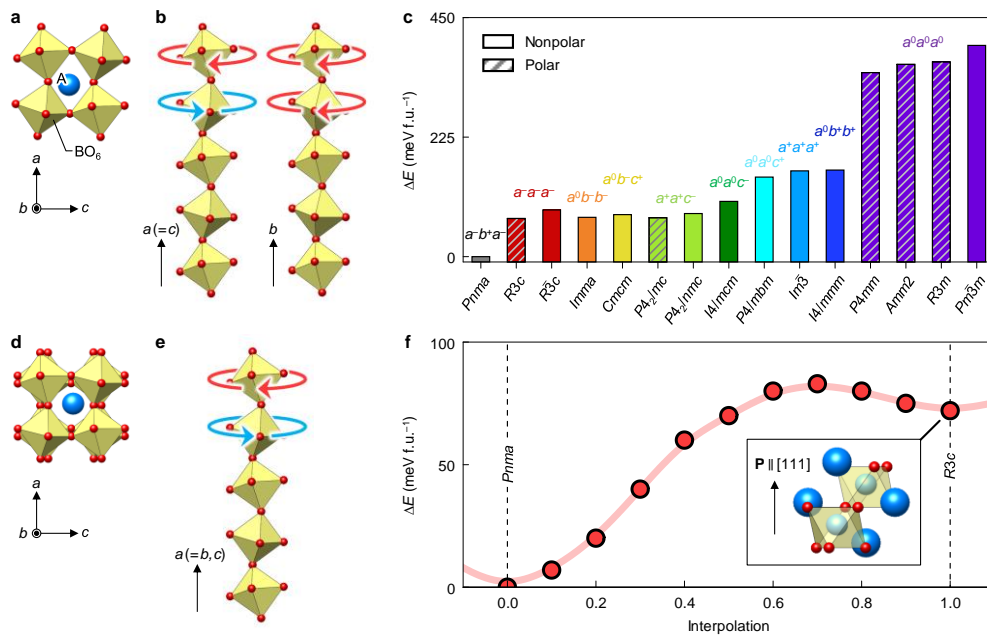


Figure 3.7 (a) Atomic structure of ABO_3 perovskite with an $a^-b^+a^-$ OOR pattern ($Pnma$). (b) $a^-b^+a^-$ OOR pattern, showing out-of-phase rotation along the a - and c -axes and in-phase rotation along the b -axis. (c) DFT calculation of the energy landscape for various OOR patterns of CaTiO_3 . The total energy for $Pnma$ is set to zero. Five structures ($R3c$, $P4_2/mc$, $P4mm$, $Amm2$, and $R3m$) are predicted to be polar. (d) Atomic structure of ABO_3 perovskite with an $a^-a^-a^-$ OOR pattern. (e) $a^-a^-a^-$ OOR pattern, showing out-of-phase rotation along all the axes. (f) Energy barrier between the $Pnma$ and metastable $R3c$ phases of CaTiO_3 .

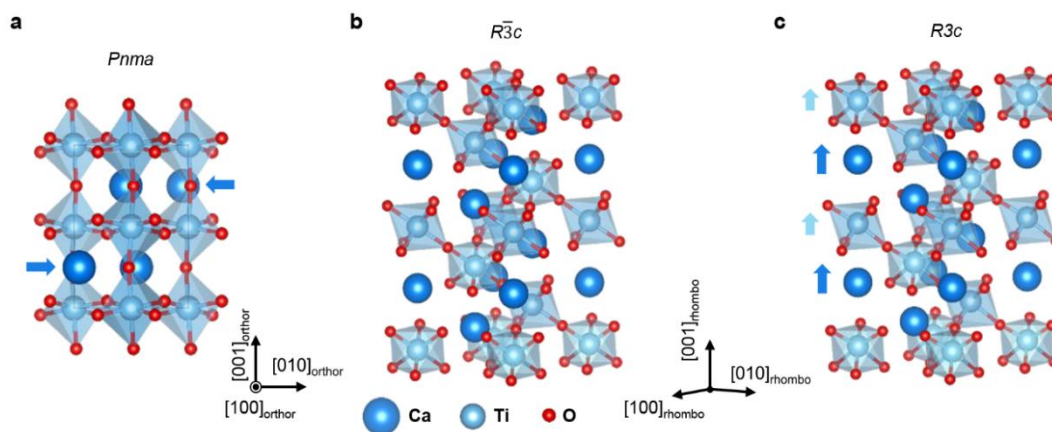


Figure 3.8 (a-c) DFT calculation of CaTiO_3 with $Pnma$ (a), $R\bar{3}c$ (b), and $R3c$ (c) structures.

3.3.2 Heteroepitaxial stabilization of metastable octahedral rotation pattern

While the $R3c$ CaTiO_3 is metastable in bulk, with a calculated energy barrier of 10 meV f.u.^{-1} [Fig. 3.7(f)], heteroepitaxial growth could make it more stable. Through simply modulating OOR angles [18], it might be difficult to convert the OOR pattern itself from $a^-b^+a^-$ (i.e., corresponding to $Pnma$) to $a^-a^-a^-$ (i.e., corresponding to $R3c$). To overcome this, we constrain CaTiO_3 to the pseudo-cubic $(111)_{pc}$ plane of the LaAlO_3 substrate, which has the $a^-a^-a^-$ OOR pattern (note that we use a pseudo-cubic unit cell throughout and omit the pc subscript hereafter). Figures 3.9(a,b) emphasize that on the (111) plane, $a^-b^+a^-$ and $a^-a^-a^-$ OORs lead to disparate lattice symmetries; among the 10 possible OOR patterns, only the $a^-a^-a^-$ pattern allows for a regular hexagon network of A-site ions. Furthermore, the (111) interface maximizes the octahedral connectivity through three

metal-oxygen-metal bonding, so that the OOR pattern of CaTiO_3 could more likely follow that of LaAlO_3 . Accordingly, coherent, epitaxial growth of CaTiO_3 films on a LaAlO_3 (111) substrate could effectively stabilize the $a^-a^-a^-$ OOR pattern [Fig. 3.8(c)] in CaTiO_3 .

We fabricate high-quality CaTiO_3 films on a LaAlO_3 (111) substrate using a pulsed laser deposition (PLD) technique. As a nonequilibrium growth method [19], PLD could assist in achieving the metastable $a^-a^-a^-$ OOR pattern in CaTiO_3 films. Atomic force microscopy and X-ray diffraction confirm that the films have smooth surfaces and high crystallinity. Previous works have reported experimental difficulties in achieving sharp, (111)-oriented heterointerfaces of perovskite oxides due to their high surface polarity [20]. In this work, we utilize *in-situ* annealing of a LaAlO_3 substrate in ultra-high vacuum to achieve an atomically sharp $\text{CaTiO}_3/\text{LaAlO}_3$ (111) interface [21]. Given this sharp interface, the OOR pattern in CaTiO_3 (111) films could follow that (i.e., the $a^-a^-a^-$ pattern) of the underlying LaAlO_3 substrate.

Using optical second harmonic generation (SHG) polarimetry, we identify the macroscopic polar point-group symmetry of CaTiO_3 (111) films. Figure 3.9(d) shows a clear SHG signal in CaTiO_3 (111) films, which best fits with the polar point group of $3m$. This is consistent with our prediction that the $\text{CaTiO}_3/\text{LaAlO}_3$ (111) heteroepitaxy could stabilize the polar $R3c$ phase with an $a^-a^-a^-$ OOR pattern in CaTiO_3 , belonging to the polar point group of $3m$. Furthermore, the SHG studies show a typical thickness dependence of ultrathin ferroelectric films. While we observe a persistent SHG signal in films thicker than 2.6 nm (i.e., 12 unit cells), the SHG signal disappears in films thinner than 1.3 nm (6 unit cells) [Fig. 3.10]. This size effect is an intrinsic characteristic in ultrathin ferroelectrics [22],

wherein ferroelectricity disappears at a finite critical thickness, e.g., due to depolarization field. Therefore, the observed SHG signal should arise solely from the bulk of CaTiO_3 (111) films, rather than from their surfaces and interfaces.

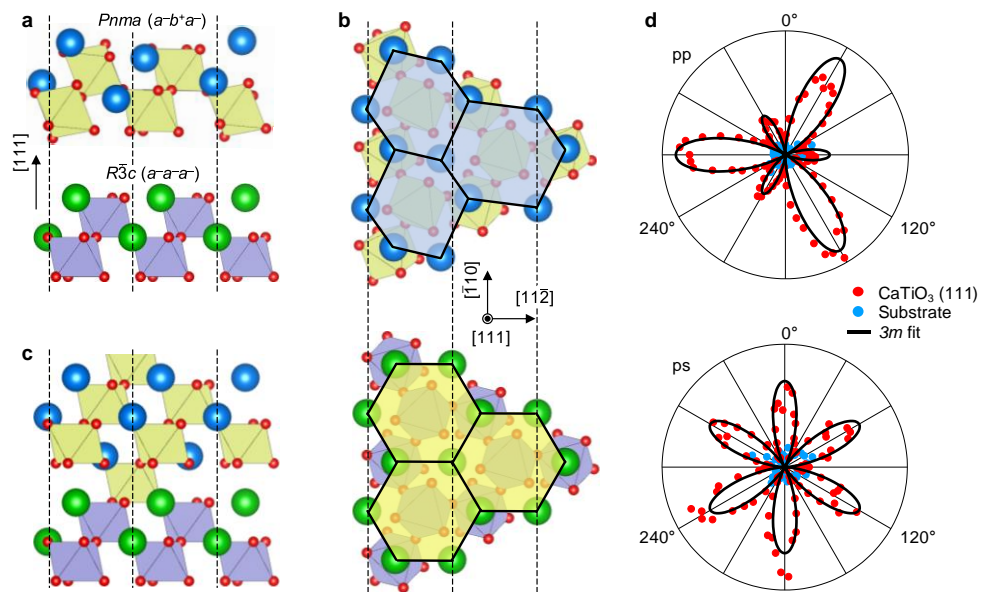


Figure 3.9 Heteroepitaxial stabilization of the $a\bar{a}\bar{a}$ OOR pattern in CaTiO_3 . (a) Structural mismatch between the $a\bar{b}^+a\bar{}$ and $a\bar{a}\bar{a}$ OOR patterns in the (111) plane. (b) Disparate in-plane lattice symmetries of the $a\bar{b}^+a\bar{}$ and $a\bar{a}\bar{a}$ OOR patterns in the (111) plane. (c) Schematic diagram of OOR pattern engineering in the (111)-oriented heterointerface between $a\bar{b}^+a\bar{}$ and $a\bar{a}\bar{a}$ structures. (d) Optical second harmonic generation (SHG) signals from 2.6 nm-thick CaTiO_3 (111) film (red) and LaAlO_3 substrate (blue). “p” (“s”) indicates parallel (perpendicular) polarization of light with respect to the plane of incidence.

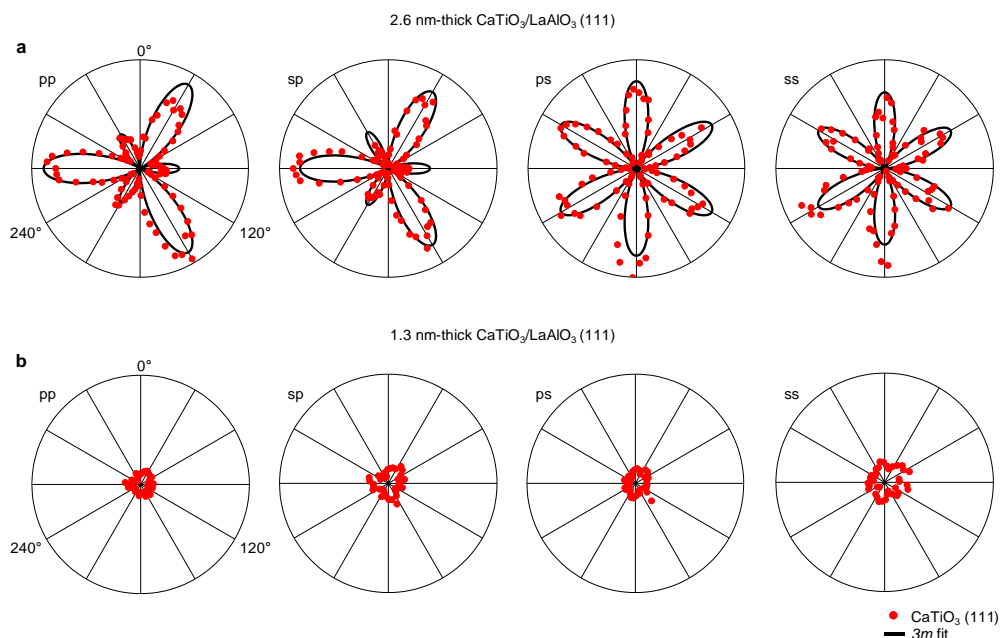


Figure 3.10 Critical thickness for ferroelectricity in CaTiO₃/LaAlO₃ (111) thin films. (a,b) Optical second harmonic generation (SHG) signals from 2.6 nm- (a) and 1.3 nm-thick (b) CaTiO₃/LaAlO₃ (111) thin films. “p” (“s”) indicates parallel (perpendicular) polarization with respect to the plane of incidence.

3.3.3 Atomic-scale visualization of oxygen octahedral rotation

Scanning transmission electron microscopy (STEM) can provide atomic-scale information on the OOR pattern, as well as ferroelectricity, of the films. In particular, annular bright field STEM (ABF-STEM) images are sensitive to light atoms (e.g., oxygen) [23], making them an effective tool for visualizing OOR patterns. Because OOR generally causes elongation of oxygen peaks in ABF-STEM images, qualitative analysis of such

elongated oxygen peaks can provide the means to identify the OOR pattern in the films [24]. Indeed, our ABF-STEM simulations, based on the calculated atomic structures in Fig. 3.7(c), indicate that each OOR pattern has its unique oxygen peak feature in the $[1\bar{1}0]$ projection: the $a^-a^-a^-$ OOR pattern has the elongated oxygen peaks aligned in one crystalline direction [Fig. 3.11(a)] and the $a^-b^+a^-$ pattern has the elongated oxygen peaks arranged in a zigzag-like pattern [Fig. 3.11(b)]. Importantly, this unique feature of the oxygen peak shapes allows the OOR pattern of the CaTiO_3 films to be identified.

Furthermore, we employ a deep neural network approach to identify the OOR patterns from the measured ABF-STEM images [25,26]. Identification of OOR patterns could be ambiguous, e.g., due to nontrivial experimental noise, difficulty in the quantification of shape information, or infinitesimal differences among OOR shapes. The deep neural network approach, however, can help us to identify OOR patterns beyond human cognition. Figure 3.11(c) displays the measured ABF-STEM image of CaTiO_3 (111) films with a zone axis of $[1\bar{1}0]$, exhibiting oxygen peaks elongated along the same direction. This is consistent with the simulated ABF-STEM image for the $a^-a^-a^-$ OOR pattern [Fig. 3.11(a)]. Our deep neural network analysis indeed identifies the $a^-a^-a^-$ OOR pattern from the measured ABF-STEM image of CaTiO_3 (111) films [Fig. 3.11(d)]. The ABF-STEM image also confirms that such an $a^-a^-a^-$ OOR pattern coexists with electric polarization in CaTiO_3 (111) films [Fig. 3.11(e)], which is in good agreement with our theoretical prediction and SHG results. Figure 3.11(e) shows rather suppressed electric polarization near the bottom interface, which might originate from interface dipoles. In stark contrast, CaTiO_3 (001) films, which differ from CaTiO_3 (111) films only in their crystalline

orientation, show the $a^-b^+a^-$ OOR pattern and no electric polarization [Fig. 3.12]. This is consistent with the nonpolar $Pnma$ phase of bulk CaTiO_3 . These results thus firmly validate our heteroepitaxial design principle for stabilizing the nonequilibrium OOR pattern and achieving polar CaTiO_3 at room temperature.

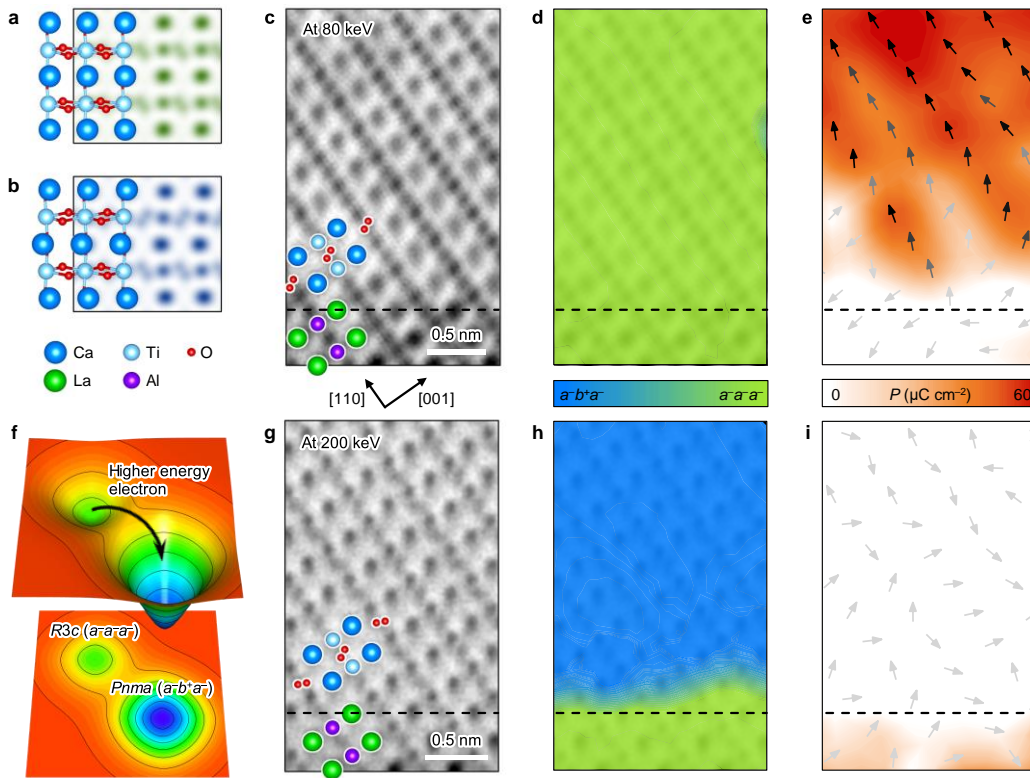


Figure 3.11 Atomic-scale analysis of the OOR pattern and polarity in CaTiO_3 films. (a,b) Simulated annular bright-field scanning transmission electron microscopy (ABF-STEM) images along the zone axis of $[1\bar{1}0]$ for $a^-a^-a^-$ (a) and $[101]$ for $a^-b^+a^-$ (b) OOR patterns. (c–i) c and g show ABF-STEM images of 2.6 nm-thick CaTiO_3 (111) film along the zone

axis of $[1\bar{1}0]$, measured using 80-keV (c) and 200-keV (g) electron kinetic energy. d and h display the maps of OOR patterns, identified by deep neural network analysis, in the same regions as in c and g, respectively. Color indicates the probability of each OOR pattern. e and i present polarization vectors for each unit cell of the same regions as in c and g, respectively. Arrows denote the polarization direction; the stronger the polarization, the darker the arrow color. Strength of polarization is also expressed as a color map, ranging from white (weak) to red (strong). f illustrates a schematic free energy landscape, showing the relaxation of $R3c$ state ($a^-a^-a^-$) into $Pnma$ state ($a^-b^+a^-$).

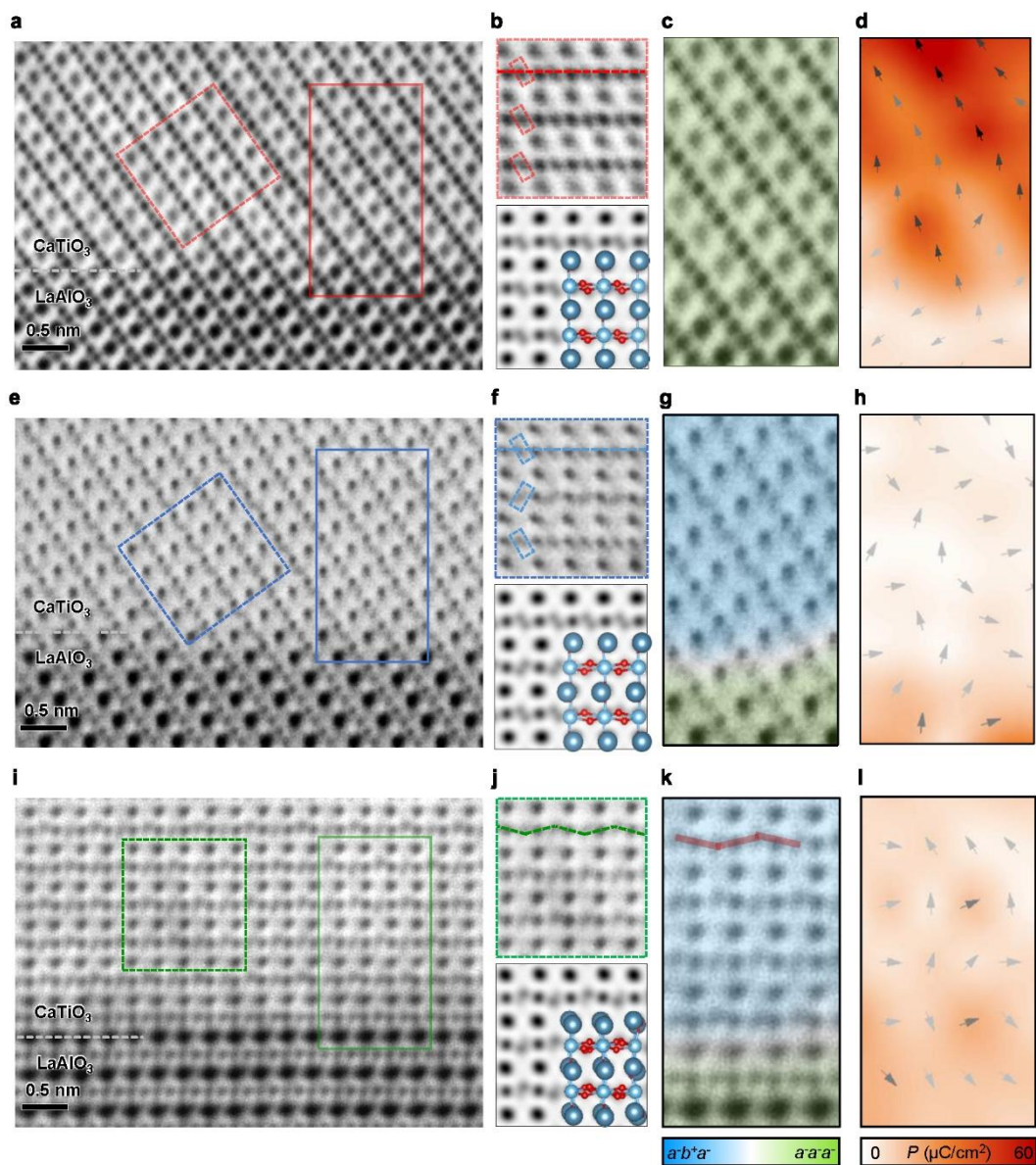


Figure 3.12 Atomic-scale analysis of the OOR pattern and polarity of the whole $\text{CaTiO}_3/\text{LaAlO}_3$ heterostructure series. (a,e) ABF-STEM image of $\text{CaTiO}_3/\text{LaAlO}_3$ (111) heterostructure along zone axis $[1\bar{1}0]$ under electron acceleration voltages of 80 kV (a) and 200 kV (e). (b) Magnified and rotated image of the red dashed box (left) in a, with the

simulated ABF-STEM image of the $a^-a^-a^-$ OOR pattern shown below. (c) A magnified image of the red solid box (right) in a and corresponding OOR pattern of each 1×2 unit cell, obtained using a convolutional neural network (CNN). Color indicates the probability (similarity) of each OOR pattern. (d) Polarization map of each unit cell in the same region as c. Arrows denote the polarization direction and intensity; the stronger the polarization, the darker the arrow. Intensity of polarization is also expressed as a color map, ranging from white (weak) to red (strong). (e) Magnified and rotated image of the blue dashed box (left) in c, with the simulated ABF-STEM image of $a^-b^+a^-$ OOR pattern shown below. (f) Magnified image of the blue solid box (right) in e and corresponding OOR map of the CNN. (g) Polarization map of the same region shown in f. (h) ABF-STEM image of $\text{CaTiO}_3/\text{LaAlO}_3$ (001) heterostructure along zone axis $[1\bar{1}0]$ under an electron acceleration voltage of 200 kV. (i) A magnified image of the green dashed box (left) in h, with the simulated ABF-STEM image of the $a^-b^+a^-$ OOR pattern shown below. (j) Magnified image of the green solid box (right) in h and corresponding OOR map of the CNN. (k) Polarization map of the same region shown in j.

3.3.4 Switchable and stable polarization at room-temperature

Then, using piezoresponse force microscopy (PFM), we examine whether the electric polarization is switchable and stable—the signature of ferroelectricity—at room temperature. To apply an electric field, we prepare CaTiO_3 films on a LaAlO_3 substrate buffered with LaNiO_3 films as the bottom electrode. Given that LaNiO_3 has the $R\bar{3}c$

structure with an $a^-a^-a^-$ OOR pattern, the same heteroepitaxy control of the OOR patterns in CaTiO_3 [Fig. 3.9(c)] would work. Our PFM measurement reveals clear hysteretic behaviour [Fig. 3.13(a,b)], with a phase difference of around 180° in CaTiO_3 (111) films, consistent with the typical ferroelectric responses under PFM. In contrast, CaTiO_3 (001) films show almost no change in the PFM phase, and a negligible PFM amplitude [Fig. 3.13(e,f)]. Accordingly, we exclude extrinsic electrochemical effects [27] as the origin of the PFM response in (111) films. Figure 3.13 verifies that the [111]-directed film growth is essential in stabilizing the ferroelectric state, as it not only guarantees the unique geometric constraint [Fig. 3.9], but also maximizes octahedral connectivity. Bipolar domain patterns [Fig. 3.13(c,d)] were writable and stable on CaTiO_3 (111) films. The pristine domain structure of CaTiO_3 (111) films was difficult to define. It could be due to the ferroelectric domain structure which can become mono-domain upon electrical poling [Fig. 3.13(c,d)].

We examined the stability of the written domains by monitoring the PFM signal as a function of time [Fig. 3.14]. The PFM signal gradually decays, following a power-law with a decay exponent of 0.145. Although comparable decay exponents have been reported in the relaxor ferroelectric phase of perovskite titanates, a similar relaxation has also been observed in prototypical ferroelectric films in ultrathin limit [28]. Based on our comprehensive DFT and STEM study, we attribute the relaxation behavior of the ferroelectric $R3c$ - CaTiO_3 to the huge depolarization field in ultrathin ferroelectric films. Taken together, our theoretical and experimental results consistently demonstrate that artificial stabilization of the nonequilibrium OOR pattern leads to robust room-temperature ferroelectricity in otherwise nonpolar CaTiO_3 films.

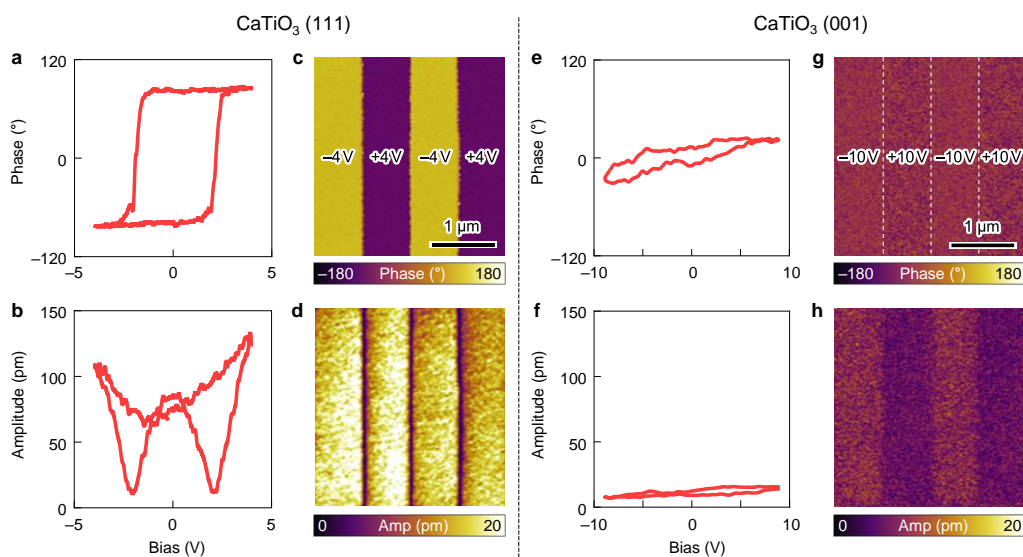


Figure 3.13 Switchable and stable polarization in CaTiO_3 (111) films. (a,b) Switching behavior of the piezoelectric phase (a) and amplitude (b) in 2.6 nm-thick CaTiO_3 (111) film. (c,d) Bipolar domain patterns, written on the same CaTiO_3 (111) film. Piezoelectric phase (c) and amplitude (d) show two stable ferroelectric domains. (e,f) Non-ferroelectric behavior of the piezoelectric phase (e) and amplitude (f) in 3.8 nm-thick CaTiO_3 (001) film. (g,h) Absence of domain patterns in the same CaTiO_3 (001) film. Piezoelectric phase (g) and amplitude (h) show absence of ferroelectric domains.

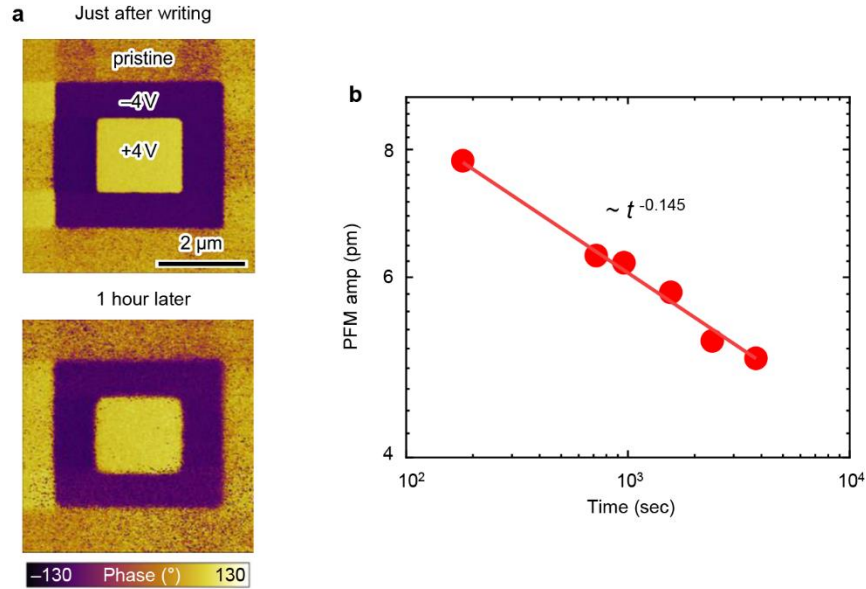


Figure 3.14 Stability of ferroelectric domain of $R3c$ - CaTiO_3 . (a) Bipolar domain of $R3c$ - CaTiO_3 which persists for an hour. (b) Time-dependent PFM amplitude of $R3c$ - CaTiO_3 which follow a power-law with an exponent of 0.145.

3.3.5 Discussion

Our results highlight that we achieve both selective stabilization and atomic-scale imaging of the ferroelectrically active, nonequilibrium $a^-a^-a^-$ OOR pattern. Importantly, because nonequilibrium states inherently involve complex structural instabilities, it has been difficult to selectively stabilize them and resolve their atomic structures [29]. However, by using the moderate conditions in the STEM experiments (e.g., electron kinetic energy of 80 keV), we successfully resolve the newly stabilized $a^-a^-a^-$ OOR pattern at the atomic scale, without structural relaxation to the ground-state ($a^-b^+a^-$ pattern). This implies that

STEM imaging with higher electron energy would cause greater perturbation of the system, possibly resulting in structural relaxation from the $a^-a^-a^-$ to the $a^-b^+a^-$ OOR pattern [Fig. 3.11(f)]. Indeed, when imaged with a higher electron kinetic energy (200 keV), the atomic structure relaxes to that of the $a^-b^+a^-$ OOR pattern, identified via deep neural network analysis [Fig. 3.11(g,h)]. Importantly, this relaxation of the OOR pattern coincides with the disappearance of electric polarization [Fig. 3.11(i)]. Furthermore, even after the OOR pattern is relaxed to $a^-b^+a^-$, CaTiO_3 still remains fully strained to the underlying LaAlO_3 substrate. This emphasizes that the epitaxial strain itself cannot stabilize the $a^-a^-a^-$ OOR pattern and resulting ferroelectricity in $\text{CaTiO}_3/\text{LaAlO}_3$ heterostructures, consistent with our DFT calculations. Thus, these results not only confirm a close correlation between the metastable $a^-a^-a^-$ OOR pattern and ferroelectricity, but also exclude the epitaxial strain as a primary origin for the ferroelectricity in CaTiO_3 (111) films.

3.4 Summary

Interest in understanding and utilizing metastable or hidden states, which would allow for exotic phenomena and functions, has been growing [29-33]. While optical pumping has been mainly used to explore nonequilibrium transient states [32], we stabilize a nonequilibrium OOR pattern and then achieve robust ferroelectricity. Our approach to utilize metastable OOR patterns for functional perovskite oxides is distinct from conventional chemical substitution [34] or strain [35] / dimensional [28] engineering. Moreover, our theory suggests that the metastable OOR pattern may facilitate the

development of novel functionalities: our results indicate that in the metastable $a^-a^-a^-$ OOR pattern, an increase in rotation angle could enhance the electric polarization [Fig. 3.15], in stark contrast to the conventional $a^-b^+a^-$ pattern (which is competitive with ferroelectricity). Such cooperation between the OOR and polar distortion could constitute a generic principle for polarizing various material systems, including not only dielectrics but also conductors. Thus, OOR pattern engineering is expected to be widely used to design novel multifunctional perovskites oxides, in which the broken inversion symmetry is combined with electron conduction, magnetism, and topological phases.

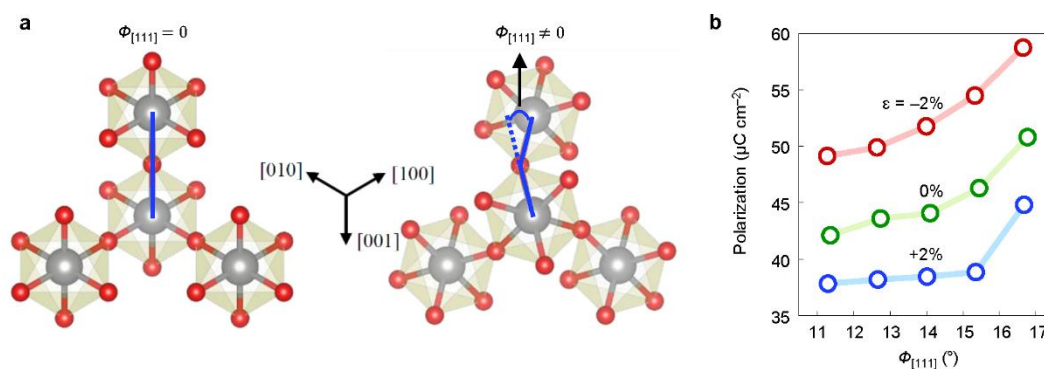


Figure 3.15 Cooperative coupling between ferroelectricity and OOR in $R3c$ - CaTiO_3 . (a) Definition of OOR angle $\Phi_{[111]}$ of $R3c$ - CaTiO_3 . (b) $\Phi_{[111]}$ - and strain-dependent ferroelectric polarization in $R3c$ - CaTiO_3 . The polarization value increases with the OOR angle, showing cooperative coupling between ferroelectricity and OOR.

References

- [1] A. M. Glazer, *Acta Cryst.* **B28**, 3384 (1972).
- [2] M. W. Lufaso and P. M. Woodward, *Acta Cryst.* **B57**, 725 (2001).
- [3] M. E. Lines and A. M. Glass, *Phys. Today* **31**, 56 (1978).
- [4] N. A. Benedek and C. J. Fennie, *J. Phys. Chem. C* **117**, 13339 (2013).
- [5] R. Ramesh and D. G. Schlom, *Nat. Rev. Mater.* **4**, 257 (2019).
- [6] J. M. Rondinelli, S. J. May, and J. W. Freeland, *MRS Bull.* **37**, 261 (2012).
- [7] H. Wang, *et al.*, *Phys. Rev. X.* **6**, 011027 (2016).
- [8] Z. Liao, *et al.*, *Nat. Mater.* **15**, 425 (2016).
- [9] Y. Shimakawa, *et al.*, *Nat. Mater.* **15**, 432–437 (2016).
- [10] T. H. Kim, *et al.*, *Nature* **533**, 68 (2016).
- [11] A. Rajapitamahuni, *et al.*, *Phys. Rev. Lett.* **116**, 187201 (2016).
- [12] M. Yashima and R. Ali, *Solid State Ionics* **180**, 120 (2009).
- [13] A. Chandra, R. Ranjan, D. P. Singh, N. Khare, and D. Pandey, *J. Phys. Condens. Matter* **18**, 2977 (2006).
- [14] E. Cockayne and B. P. Burton, *Phys. Rev. B* **62**, 3735 (2000).
- [15] V. V. Lemanov, A. V. Sotnikov, E. P. Smirnova, M. Weihnacht, and R. Kunze, *Solid State Commun.* **110**, 611 (1999).
- [16] P. M. Woodward, *Acta Cryst.* **B53**, 44 (1997).
- [17] D. I. Bilc, *et al.*, *Phys. Rev. B* **77**, 165107 (2008).
- [18] A. J. Hatt and N. A. Spaldin, *Phys. Rev. B* **82**, 195402 (2010).

- [19] K. Hanzawa, M. Sasase, H. Hiramatsu, and H. Hosono, *Supercond. Sci. Technol.* **32**, 054002 (2019).
- [20] J. L. Blok, X. Wan, G. Koster, D. H. A. Blank, and G. Rijnders, *Appl. Phys. Lett.* **99**, 151917 (2011).
- [21] J. R. Kim, *et al.*, *Phys. Rev. Mater.* **3**, 023801 (2019).
- [22] J. Junquera and P. Ghosez, *Nature* **422**, 506 (2003).
- [23] R. Ishikawa, *et al.*, *Nat. Mater.* **10**, 278 (2011).
- [24] Q. He, *et al.*, *ACS Nano* **9**, 8412 (2015).
- [25] Y. Rivenson, *et al.*, *Optica* **4**, 1437 (2017).
- [26] M. Ziatdinov, *et al.*, *ACS Nano* **11**, 12742 (2017).
- [27] S. M. Yang, *et al.*, *Nat. Phys.* **13**, 812 (2017).
- [28] D. Lee, *et al.*, *Science* **349**, 1314 (2015).
- [29] V. A. Stoica, *et al.*, *Nat. Mater.* **18**, 377 (2019).
- [30] R. Mankowsky, *et al.*, *Nature* **516**, 71 (2014).
- [31] M. Buzzi, M. Först, R. Mankowsky, and A. Cavalleri, *Nat. Rev. Mater.* **3**, 299 (2018).
- [32] X. Li, *et al.*, *Science* **364**, 1079 (2019).
- [33] D. Lee, *et al.*, *Science* **362**, 1037 (2018).
- [34] T. Mitsui and W. B. Westphal, *Phys. Rev.* **124**, 1354 (1961).
- [35] J. H. Haeni, *et al.*, *Nature* **430**, 758 (2004).

Chapter 4

Demonstration of controllable electronic structures at oxide heterointerfaces

Despite huge interest on emergent phenomena at oxide interfaces, direct observation of the interfacial electronic phases has been challenging due to experimental limitations. We combined atomic-scale epitaxy of artificial oxide heterostructures and in situ angle-resolved photoemission spectroscopy (ARPES) to experimentally demonstrate the ‘interface control of electronic structures’ at oxide interfaces. We attribute the limited length scale of the interface effect as the origin for the experimental difficulties so far. In this work, we selected untrathin SrRuO₃ epitaxial films which has metallic property down to the single-atomic-layer limit and therefore becomes an ideal platform to realize the controllable electronic structures. We fabricated heterointerfaces between atomically thin SrRuO₃ and a variety of perovskite titanate (CaTiO₃, SrTiO₃, BaTiO₃). Those titanates impose various structural distortions into the atomically thin SrRuO₃ layers such as oxygen octahedral rotation and ferroelectricity. The structural distortion effectively controlled the electronic structures of the atomically thin SrRuO₃ and realize a crossover between Mott insulator, incoherent metal, and Fermi liquid.

4.1 Background

4.1.1 Emergent phenomena at oxide interfaces

Complex transition metal oxides have a wide range of physical properties and high integrity in heterostructures. Thanks to the recent advancement of thin film deposition technique, atomically controlled oxide interfaces now offer a variety of novel physics including a two-dimensional electron gas at $\text{LaAlO}_3/\text{SrTiO}_3$ heterointerface, interfacial ferromagnetism, and orbital reconstruction [1-3].

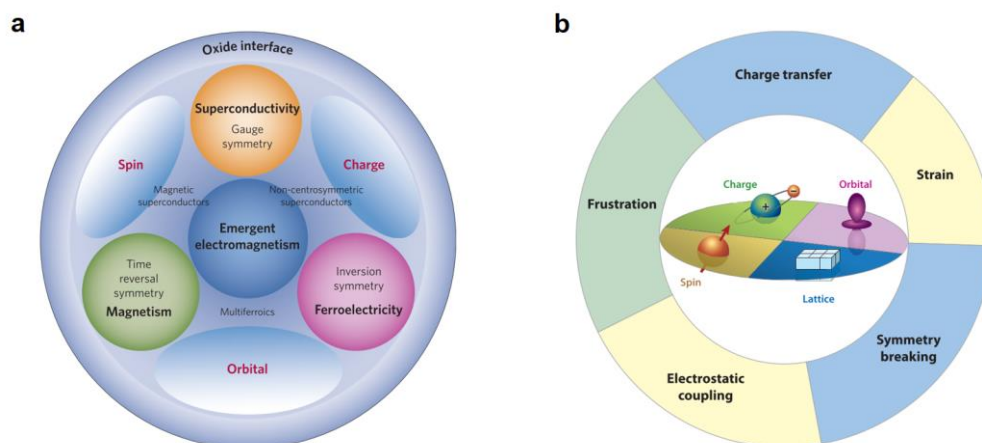


Figure 4.1 (a) Symmetries and degrees of freedom of correlated electrons at oxide interfaces. (b) Interaction of the physical degrees of freedom through symmetry breaking, charge transfer, electrostatic coupling, strain, and frustration. Adapted from [2,3].

At the oxide interfaces, charge, spin, orbital, and lattice degrees of freedom in the correlated electron systems interact through numerous interface effects such as local symmetry breaking, charge transfer, electrostatic coupling, strain, and frustration [Fig. 4.1]. As a result, the interface physics of the oxide heterostructures is very complicated, and the control of the interfacial electronic phases and direct experimental characterization should be of great interest. However, the characterization of the interfacial electronic structures has been largely limited by the short length scale of the interfacial phenomena.

4.1.2 Metal-insulator transition in ultrathin oxide films

In the atomically-thin limit of the films, the reduced dimension can impose a different boundary condition to the film materials and possibly change the electronic structure. In case of the transition metal oxide thin films, known materials have shown metal-insulator transition in the ultrathin limit [4-6, Fig. 4.2]. Localization, quantum confinement, and enhanced Coulomb interactions in the low dimension have been proposed as the origin of the metal-insulator transition. Indeed, this monotonous insulating behavior of the ultrathin transition metal oxide thin films also restricts the exploration of the interfacial electronic structures. The reason is that the interface effects are usually in the range of several atomic layers from the interface. If a low-dimensional electronic oxide can be realized, direct experimental observation of the interfacial electronic structures will be possible based on the enhanced interfacial coupling.

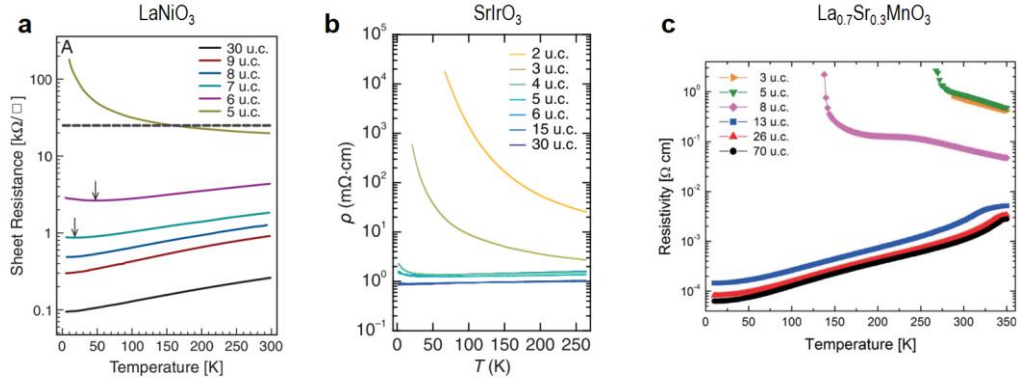


Figure 4.2 (a-c) Metal-insulator transition in ultrathin films of LaNiO₃ (a), SrIrO₃ (b), and La_{0.7}Sr_{0.3}MnO₃ (c). Adapted from [4-6].

4.1.3 Motivation

In this chapter, we aim to demonstrate the interface control of electronic structure using a metallic single-atomic-layer oxide. To discover the metallic single-atomic-layer oxide and probe the controllable electronic structure, we employed angle-resolved photoemission spectroscopy (ARPES) [Fig. 4.3(a)]. We established *in situ* PLD-ARPES system where the PLD-grown films can be transferred to the ARPES system without breaking the vacuum [Fig. 4.3(b)]. In the ultrathin limit, increased scattering from the surface and interface gives additional extrinsic factors in the conventional transport measurement. Directly detecting the electronic states in the periodic lattices, the ARPES would resolve the intrinsic properties of the ultrathin oxide films and become an ideal experimental tool for our study.

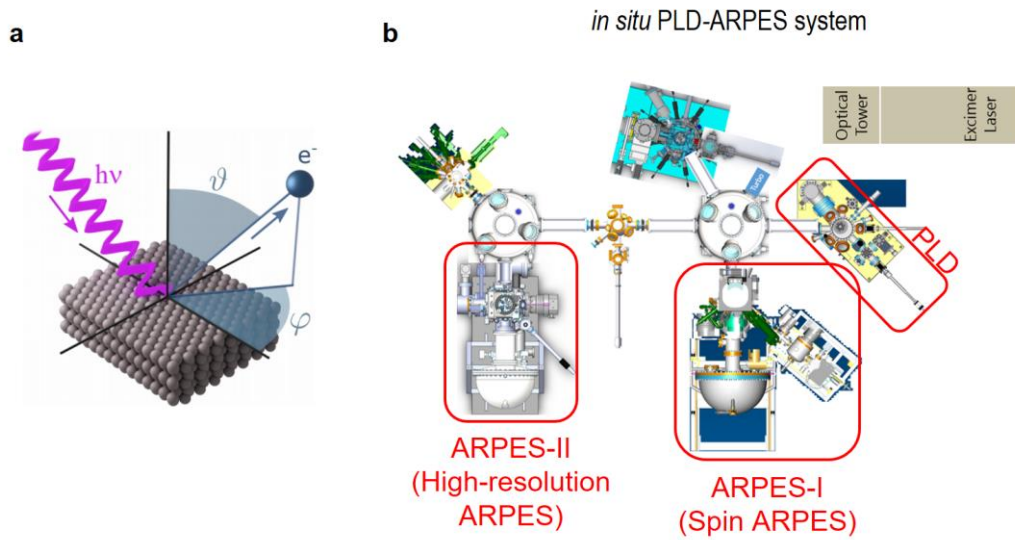


Figure 4.3 (a) Schematic description of angle-resolved photoemission spectroscopy (ARPES). (b) Schematic description of *in situ* PLD-ARPES system.

4.2 Observation of a metallic single-atomic-layer oxide

Two-dimensional (2D) materials and their electronic phases have been a core of condensed matter physics in the past decade. Associated devices [7], heterostructures [8], and Moiré superlattice [9,10] have created unique physics and substantial functionalities. However, oxide has been out of scope in the study of 2D materials due to technical difficulties in the preparation and characterization of such systems. The strong electronic

correlation characteristic of transition metal oxides causes additional complexity in resolving the electronic structures of the 2D oxide. The strong correlation, though, is also the source of a wide variety of emergent phenomena, such as high-temperature superconductivity, Mott transitions, ferromagnetism, and so on [11–13]. Thus, the realization of the 2D oxide electronic system will enable the integration of the strongly correlated electron into the field of 2D materials.

Since most oxides have strong ionic or covalent bonds, mechanical exfoliation techniques as in the case of van der Waals materials are limited in most oxides. Accordingly, epitaxial thin film growth must be implemented to construct 2D oxides. Numerous experiments have been carried out on epitaxial oxide thin films with varying thickness. Yet, to the best of our knowledge, all these reports have shown metal-insulator transition in the reduced thickness [4–6], and strong-correlation-induced Mott insulating phases have often been discussed. Such monotonous behavior limits the functional spectrum of 2D oxides, hence a metallic 2D oxide should be demonstrated to extend the range of properties and possible applications.

To search for the metallic 2D oxide, we first require an effective means to detect the electronic phases of 2D oxides. It should be noted that thin films usually suffer from deterioration in quality. For example, mechanically exfoliated graphene has the highest quality, whereas epitaxial graphene thin films prepared by the chemical vapor deposition method show lower mobility and higher density of defects [14]. As the 2D oxides are limited to thin films, the high density of defects must be seriously considered in

characterizing the material properties. In that sense, conventional transport measurement is not a proper tool for 2D oxides, since weak or strong localization can occur in disordered electronic systems [15]. Such extrinsic effects tend to be more pronounced in the reduced thickness due to increased scattering from interfaces and surfaces [16]. Here, we adapted angle-resolved photoemission spectroscopy (ARPES) to investigate the electronic phases of 2D oxides. As a direct method to obtain electronic band structures, ARPES might minimize any extrinsic contributions from the disorders and become the most effective approach to unveil the hidden phases of 2D oxides.

There have been several ARPES studies on ultrathin epitaxial transition metal oxide films [17–21]. For the case of SrIrO_3 and LaNiO_3 , the study has even reached the monolayer limit, where insulating electronic structures have been observed. We noticed a similarity between the monolayer oxide films and their quasi-two-dimensional counterparts; Both Sr_2IrO_4 [22] and NdSrNiO_4 [23] are antiferromagnetic insulators. Based on this analogy, we selected a single-atomic-layer-thick SrRuO_3 (SRO) film [Fig. 4.4(a)], a two-dimensional analogue of a metallic layered perovskite Sr_2RuO_4 [24].

4.2.1 Design of charging-free ultrathin SrRuO₃ heterostructures

We fabricated high-quality and charging-free ultrathin SRO heterostructures with varying thickness. Figure 4.4(b) shows the schematic of the SRO heterostructure which consists of 4 unit cell (uc) SRO layer, 10 uc SrTiO₃ (STO) buffer layer, and n uc ultrathin SRO layer, sequentially grown on STO (001) substrate. In our ARPES measurement, escaping photoelectrons left a charging effect on a sample and distorted measured spectra [Fig. 4.5]. By introducing the conducting layer of 4 uc SRO layer, we successfully removed the charging effect in the ultrathin SRO [Fig. 4.4(c)]. The 10 uc STO buffer layer isolates the topmost ultrathin SRO film from the conducting layer.

Scanning transmission electron microscopy (STEM) provides atomic-scale visualization of our charging-free ultrathin SRO heterostructures. Figure 4.4(d) displays a cross-sectional high-angle annular dark-field STEM (HAADF-STEM) image with STO [100] zone axis. To image the monolayer SRO, we deposited an additional 10 uc STO capping layer to protect the monolayer SRO. The conducting layer, buffer layer, monolayer SRO, and capping layer are well organized in the preferred order. In the plot of HAADF-STEM intensity across the monolayer SRO and adjacent interfaces [Fig. 4.4(e)], an abrupt Ru peak out of the surrounding Ti peaks are evident. The abrupt SRO/STO interfaces are further corroborated by energy-dispersive X-ray spectroscopy (EDS) analysis [Fig. 4.4(f)]. Taken together, we confirmed that our ultrathin SRO layers possess lateral uniformity and atomically sharp interfaces, which will allow for a systematic ARPES study.

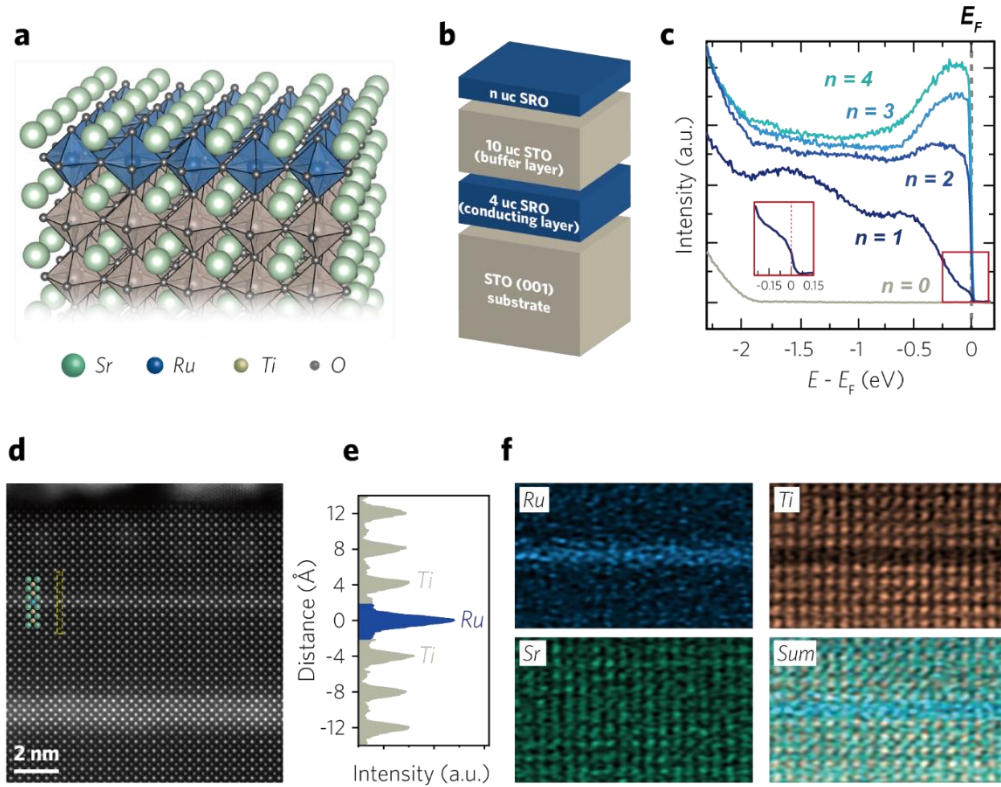


Figure 4.4 Observation of a metallic single-atomic-layer oxide in charging-free ultrathin SrRuO₃ (SRO) heterostructures. (a) A schematic of a monolayer SRO grown on a (001)-oriented SrTiO₃ (STO) layer. (b) A schematic of charging-free ultrathin SRO heterostructure. The conducting layer prevents charging effect during photoemission measurement. The buffer layer isolates the ultrathin SRO layer from the conducting layer. (c) Angle-integrated photoemission spectra from charging-free ultrathin SRO heterostructures. Energy distribution curves (EDCs) are integrated in a range of $-0.6 \text{ \AA}^{-1} < k_x < 0.6 \text{ \AA}^{-1}$ and $k_y = 0$. n indicates the number of SRO layer. Fermi edge is persistent down to the monolayer. The inset shows magnified spectra of the monolayer SRO near Fermi

level. (d) Atomic-scale imaging of the charging-free monolayer SRO heterostructure using high-angle annular dark-field scanning transmission electron microscopy (HAADF-STEM). (e) HAADF-STEM intensity across the monolayer SRO and adjacent interfaces. (f) Atomic-scale chemical analysis on the charging-free monolayer SRO heterostructure.

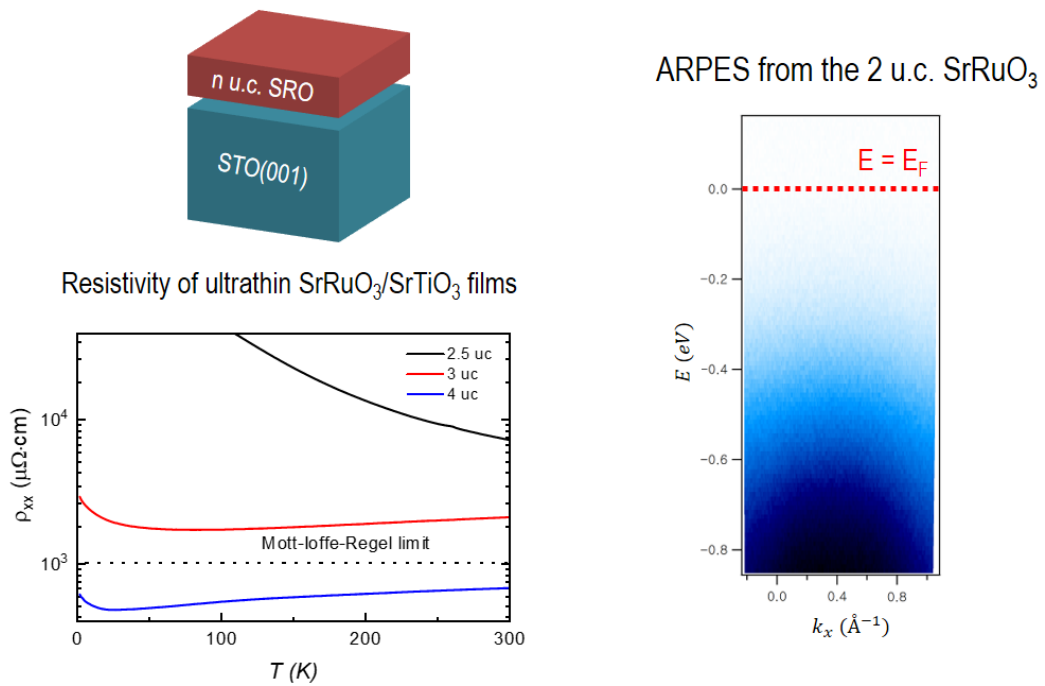


Figure 4.5 Characterization single layer SRO films. Below the 3 uc thickness, the SRO films show insulating transport behavior. When ARPES measurement is carried on the insulating sample, no spectra are observed near the Fermi level.

4.2.2 Thickness-dependent electronic structures of ultrathin SrRuO₃ films

Using the charging-free ultrathin SRO heterostructures, we examine an electronic ground state of the monolayer SRO. We performed in-situ ARPES on the heterostructures with $n = 0, 1, 2, 3,$ and 4 uc. Figure 4.4(c) shows angle-integrated photoemission spectra from the heterostructures near Γ . Definite Fermi edges survive down to monolayer, showing the persistent density of states (DOSs) at the Fermi level. A pronounced spectral weight is observed near the Fermi level of 4 and 3 uc SROs, consistent with the thick SRO film, reported previously [25]. As the thickness reduced, the spectral weight shifts toward high-binding energy, resulting in only a weak Fermi level spectrum in the 1 uc SRO. While the underlying mechanism for the peak shift is ambiguous, we clearly observed a metallic ground state of the monolayer SRO.

For fundamental understanding on this metallic monolayer SRO, we look into the Fermi surfaces (FSs) of the ultrathin SRO with varying thickness [Fig. 4.6(a)]. Consistent with the angle-integrated photoemission results [Fig. 4.4(c)], metallic FSs are resolved down to the monolayer as well. Here, we define three bands at the FSs as α , β , and γ , shown in Fig. 4.6(b). In the FSs of 4 and 3 uc SRO [Fig. 4.6(a)], sharp α and β bands, but a broad γ band are seen. In the 2 and 1 uc, even α and β bands slightly broaden as well, possibly due to the small Fermi-level spectral weight. Still, FSs do not show qualitative change with varying thickness.

Density functional theory (DFT) calculation of 2D SRO reproduces the

characteristic band structures of experimentally observed FSs [Fig. 4.6(b)]. The van Hove singularity (VHS) of the γ band is located at the X point. The broad spectral weight at the X point on the $k_y = 0$ line [Fig. 4.6(a)] indicates that the VHS of our ultrathin SRO layers lies close to the Fermi level. Note that since the ARPES data are measured with linear vertical (LV) polarized He I α light, the spectral weight can be weakly observed near the X point on the $k_x = 0$ line [26].

We first discuss the thickness-dependent evolution of α and β bands, which are mainly composed of out-of-plane orbitals, d_{xz} and d_{yz} . Figure 4.6(c) shows Γ -M high-symmetry cuts and momentum distribution curves (MDCs) at the Fermi level of each SRO layers [Cut 1 in Fig. 4.6(a)]. We detected only two band dispersions in the Γ -M cut of the 2 and 1 uc SRO, despite the existence of three bands. As we will discuss later, we can exclude the gamma band from this cut, and assign two dispersions to α and β bands located near the $k_{\parallel} = 0.6$ and 0.8 \AA^{-1} , respectively. The α band, marked with an inverted triangle in the MDCs, is resolved at Fermi level regardless of the thickness [upper panel, Fig. 4.6(c)]. Putting it all together, the characters of the α and β bands are quite independent of the thickness, but those gradually become less coherent as the thickness is reduced.

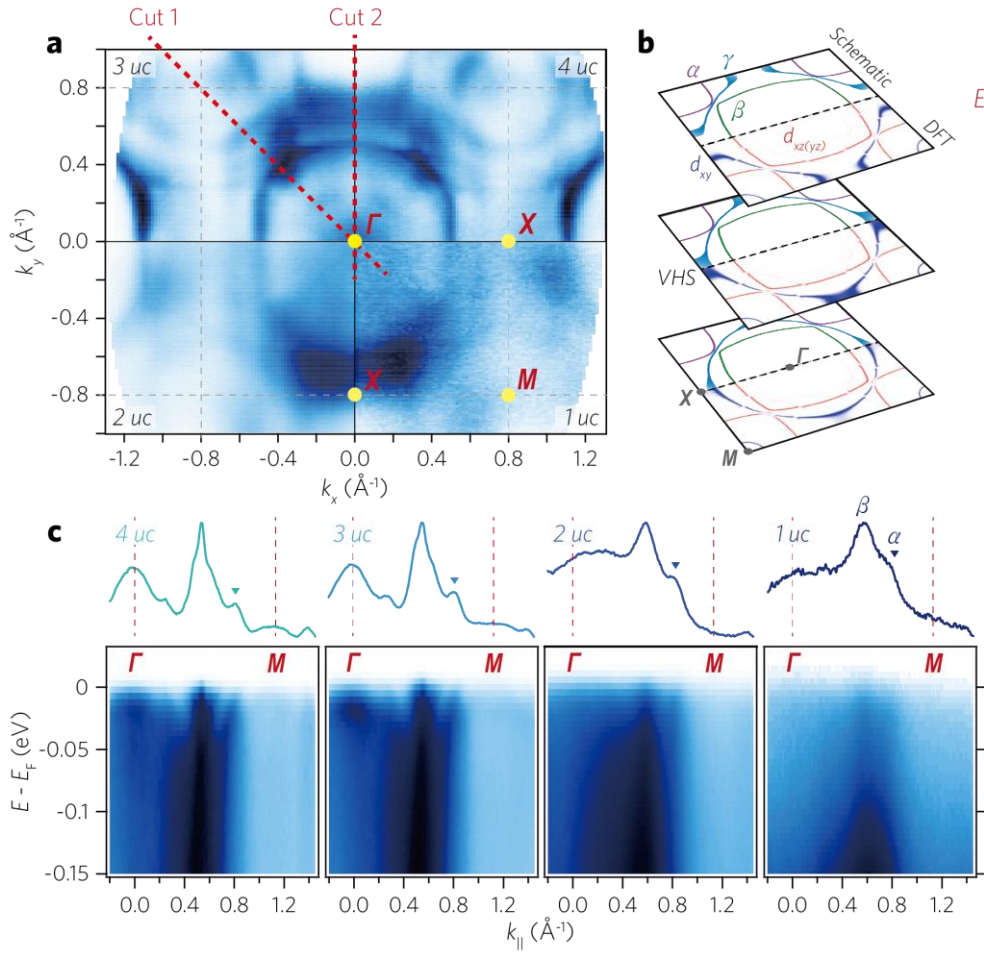


Figure 4.6 Fermi surfaces (FSs) of ultrathin SRO films. (a) FSs of ultrathin SRO layers with specified thickness. ARPES data were taken at 10 K with He-I α light (21.2 eV) and integrated within $E_F \pm 10$ meV. (b) Energy isosurfaces of two-dimensional (2D) SRO calculated by density functional theory (DFT) calculation, together with schematic energy isosurfaces. (c) Γ -M high-symmetry cuts [Cut 1 in (a)] and momentum distribution curves (MDCs) at the Fermi level (E_F). The inverted triangles in MDCs represent peaks of a α band. Both α and β bands are resolved in 1 uc.

4.2.3 Electronic coherency and magnetism in ultrathin SrRuO₃ films

The FS analysis is not enough to understand the thickness-dependent spectral-weight transfer in the ultrathin SROs. To clarify the origin, we now turn our attention to the γ band whose VHS at the X point seemingly lies close to the Fermi level. The VHS possesses high DOS which induces strong electronic correlations [Fig. 4.7(a)]. Thus, it is worth to examine the electronic band structures near the VHS. Figure 4.7(b) shows background-subtracted E - k dispersions along the $k_x = 0$ line [Cut 2 in Fig. 4.6(a)]. In the 4 and 3 uc, a coherent heavy γ band, as well as a β band, is clearly observed, whereas the 2 and 1 uc SROs show only an incoherent γ band. Note that considering the α and β bands remain consistently coherent at the FSs [Fig. 4.6(c)], we guess that the spectra of the β band are hidden behind the broad γ band.

The thickness-dependent evolution of the γ band is manifested by analyzing energy distribution curves (EDCs) at $(k_x, k_y) = (0, 0.75)$ [Fig. 4.7(c)]. The coherent peak (inverted triangles) appears as a kink in the EDCs, shown in the 4 and 3 uc SRO. However, the coherent peak disappears in the 2 and 1 uc SRO and, probably, the spectral weight is transferred to the incoherent band. Such behavior is reminiscent of the strongly correlated metal such as cuprates [27]. Based on this EDC analysis, it can be deduced that the thickness-dependent electronic transition is closely related to the strongly correlated γ band. Accordingly, we could refer to the monolayer SRO is an orbital-selectively correlated,

incoherent metal.

While bulk SRO is ferromagnet [28], its quasi-2D analogue, Sr_2RuO_4 , do not show ferromagnetism [24]. It implies a possible magnetic transition in the ultrathin SROs. We investigated the spin polarization of each ultrathin SROs by performing spin-resolved ARPES (SARPES). Figure 4.7(d) shows the spin-resolved EDCs measured at 10 K near Γ . We obtained different intensities between majority and minority spins from the 4 and 3 uc SRO, showing ferromagnetism. However, the ferromagnetism is not observed in the 2 and 1 uc SROs, where there is no difference in SARPES data. Note that our result ascertains the quantum confinement (QC) effect of ultrathin SRO films [29]. With only a few layers, the reduced dimensionality affects the bands with out-of-plane orbital characters, d_{xz} and d_{yz} . In the process, Fermi level DOS is reduced and thus ferromagnetism is lost.

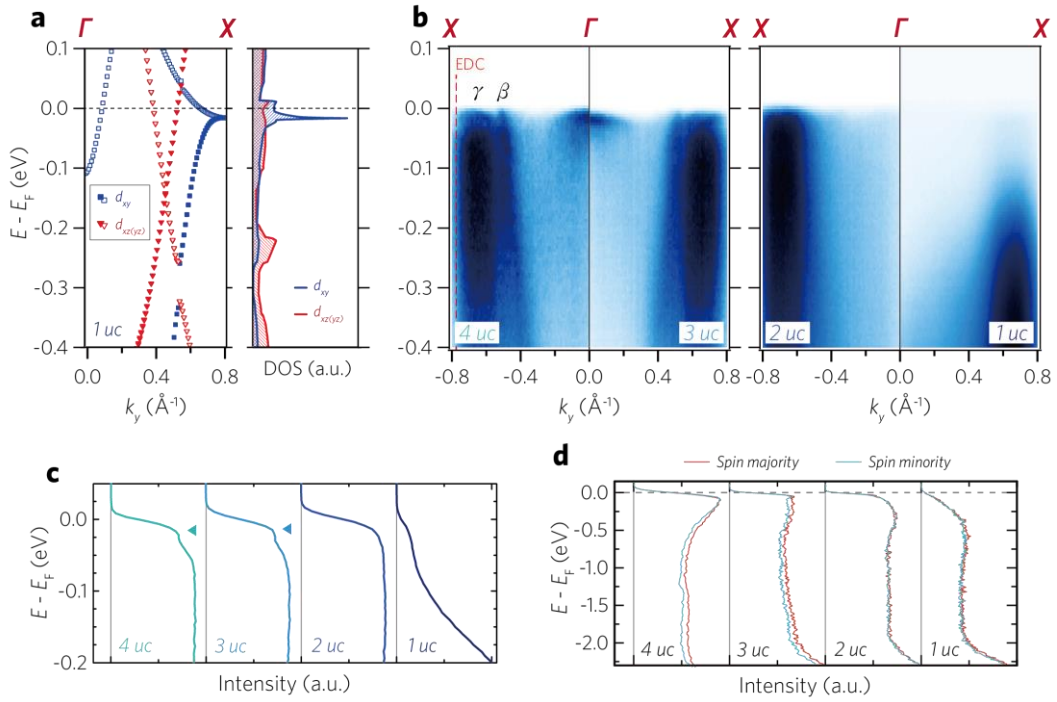


Figure 4.7 Thickness-driven electronic and magnetic transition in ultrathin SRO layers. (a) A DFT-calculated energy versus momentum ($E-k$) dispersion of 2D SRO along Γ -X high-symmetry line. (b) Background-subtracted high-symmetry cuts (Γ -X) with specified thickness of SRO layers along the $k_y = 0$ line. Coherent β and γ band dispersions are observed in 4 and 3 uc, whereas only an incoherent γ is observed in 2 and 1 uc. (c) Thickness-dependent energy distribution curves (EDCs) at $(k_x, k_y) = (0, 0.75)$ marked with a red dotted line in (b). Inverted triangles indicate coherent peaks of the γ band. The coherent peaks systematically disappear as the thickness reduced. (d) Thickness-dependent spin-resolved EDCs measured at 10 K near Γ . The spectra of spin majority and minority are different in 4 and 3 uc, whereas the difference goes zero in 2 and 1 uc

4.2.4 Interplay between dimensionality, electronic correlation, and magnetism

We noticed a remarkable coincidence between the band coherency and magnetism in the ultrathin SROs. Both coherent-to-incoherent and ferromagnetic-to-nonmagnetic transitions start to occur at the 2 uc thickness, which suggests a strong interplay between electronic correlation and magnetism.

In three-dimensional (3D) cubic SRO, three $t2g$ orbitals, (d_{xy} , d_{yz} , and d_{xz}) degenerates. Our DFT calculation [Fig. 4.7(a)] shows that, in SRO grown on STO (001), compressive epitaxial strain and oxygen octahedral rotation (OOR) lift the degeneracy and VHS of the d_{xy} band lies slightly below the Fermi level [30]. The high DOSs from the VHS [Fig. 4.8(b)] can give rise to the strong correlation effect such as Coulomb interaction and Hund's coupling [31]. The VHS at the Fermi level can be avoided as the d_{xy} band splits into spin majority and minority bands, as shown in the 4 and 3 uc SRO. In the 1 and 2 uc SRO, however, the QC effect on the d_{yz} and d_{xz} bands reduces the DOS, and inhibits the transition to the ferromagnetic phase. Meanwhile, the VHS of the d_{xy} band remains near the Fermi level. Thus, without the spin splitting, the strong correlation results in the incoherent metallic phase of the monolayer SRO [Fig. 4.8(c)].

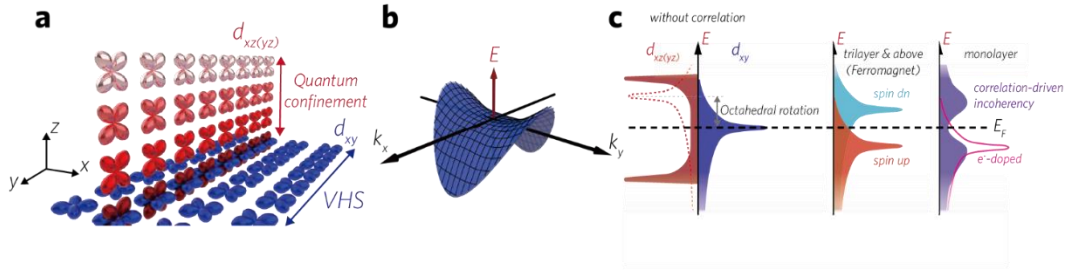


Figure 4.8 Interplay between dimensionality, electronic correlation and magnetism. (a, b) Schematic description of quantum confinement (QC) effect and van Hove singularity (VHS). The out-of-plane orbitals, d_{xz} and d_{yz} are mainly involved with the QC effect. The in-plane orbital, d_{xy} , is responsible for the high DOS, which is produced by van Hove singularity (VHS) near the Fermi level. (c) Schematic description of the electronic density of states (DOSs) depending on the orbital and thickness. The VHS of d_{xy} gives rise to the strong electronic correlation. In thick films (more than 3 uc), the VHS can be avoided by ferromagnetic spin splitting. In monolayer SRO, the spin splitting is inhibited due to the QC effect, and quasi-particle coherency is strongly suppressed. When VHS is far from the Fermi level, coherent states can be recovered.

4.2.5 Charge modulation of the monolayer SrRuO₃

After clarifying the thickness-driven electronic transition, we would like to control the electronic phases of the monolayer SRO. The key to the incoherent-metallic phases is the VHS. Hence, tuning the chemical potential is likely to break the correlated phases [Fig.

4.8(c)]. We carried out in-situ K dosing to dope electrons into the incoherent metal monolayer SRO. Figure 4.9(a) shows a FS of the monolayer SRO after K dosing. The k_F of the β band changes from 0.52 to 0.60 \AA^{-1} along the $k_x = 0$ line, indicating that electrons are doped into the monolayer SRO. Note that, compared with the pristine sample [Fig. 4.6(a)], the FS is much better resolved. The most distinct change is the γ band, which has never been coherently observed in the pristine FS, but now appears [Fig. 4.9(b)]. The Fermi level of the electron-doped monolayer SRO seems to be located above the VHS [Fig. 4.6(b)].

Notably, the electron-doped monolayer SRO has been identified as a Fermi liquid phase. Figure 4.9(b) shows background-subtracted E - k band dispersions along the $k_x = 0.2$ \AA^{-1} line before and after K dosing. The electron doping effectively transfers the spectral weight from the incoherent to the coherent peaks. EDCs in Fig. 4.9(c) depict the spectral-weight transfer and concurrently shows the emergence of the coherent quasi-particle peak near the Fermi level.

Some remarks would be given concerning the electron-doped single-atomic-layer SRO. First, we can exclude the possibility of extrinsic disorder as an origin for the incoherent metallicity of the monolayer SRO. If the incoherent metallicity were due to defects, it would have been persistent after K dosing. The reappearance of coherent peak with K dosing supports the intrinsic properties of the observed monolayer SRO. Second, the K-dosing highlights both the rich electronic spectrum of the monolayer SRO and its giant tunability by charge modulation. The considerable spectral weight and Fermi liquid properties implies a good metallicity of the electron-doped monolayer SRO. The

incoherent-coherent crossover might be exfoliated to realize novel two-dimensional field-effect-transistors, which has never been realized in the 2D oxide yet.

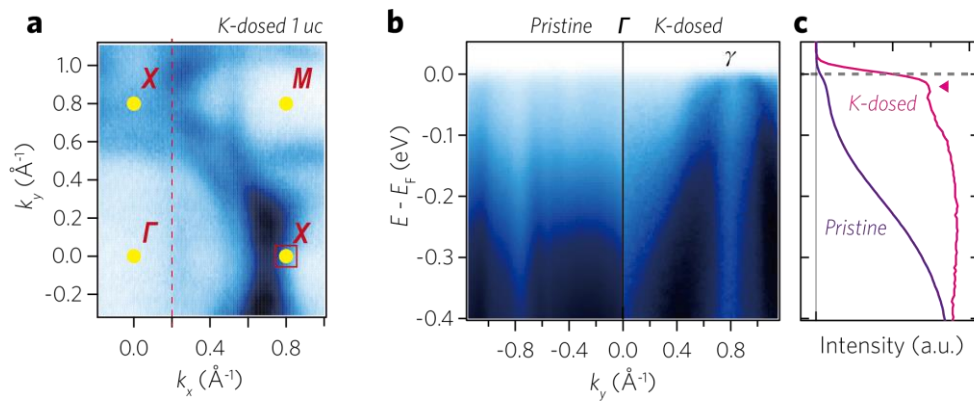


Figure 4.9 Crossover from incoherent metal to Fermi liquid in monolayer SRO. (a) FS of K-dosed monolayer SRO measured at 10 K. (b) Background-subtracted cut of pristine and K-dosed monolayer SROs along the $k_x = 0.2$ line [Red dotted line in (a)]. (c) EDCs of pristine and K-dosed monolayer SROs at X point [Red square in (a)]. With K dosing, a quasi-particle peak appears near the Fermi level marked by an inverted triangle.

4.3 Interface control of electronic structures in ultrathin oxide heterostructures

4.3.1 Interface control of octahedral distortion

Based on the metallic single-atomic-layer oxide, monolayer SrRuO₃, we attempt to control its electronic structure by interface engineering. The minimum unit of the materials promises the maximum interfacial tenability in the electronic structures. As we discussed in previous chapters, three-dimensionally connected corner-shared octahedra gives giant structural coupling at the perovskite oxide heterointerfaces. Here, we controlled the octahedral distortion of the atomically thin SRO by changing the underlying buffer layer [Fig. 4.4(b)] from STO to other perovskite titanates. The family of perovskite titanates ATiO₃ (ATO, A = Ca, Sr, and Ba) has OOR, cubic structure, and ferroelectricity, respectively, at room-temperature. At the SRO/CTO interface, the CTO induces the orthorhombic $a^-b^+a^-$ OOR pattern to the SRO layers and alters magnetic anisotropy [32]. At the SRO/STO interface, the ultrathin SRO films (< 20 uc) adopt the tetragonal $a^0a^0c^-$ OOR pattern [33]. At the SRO/BTO interface, a ferroelectric proximity effect occurs. The ferroelectric polarization of the BTO layer can penetrate into the several unit cell of the SRO layer, controlling the magneto-transport property of the ultrathin SRO films [34]. Figure 4.10 schematically displays the expected octahedral configurations of each monolayer SRO/ATO heterointerface. Investigation on the three distinct interfaces would clarify how each octahedral distortion affects the electronic structures of perovskite oxides.

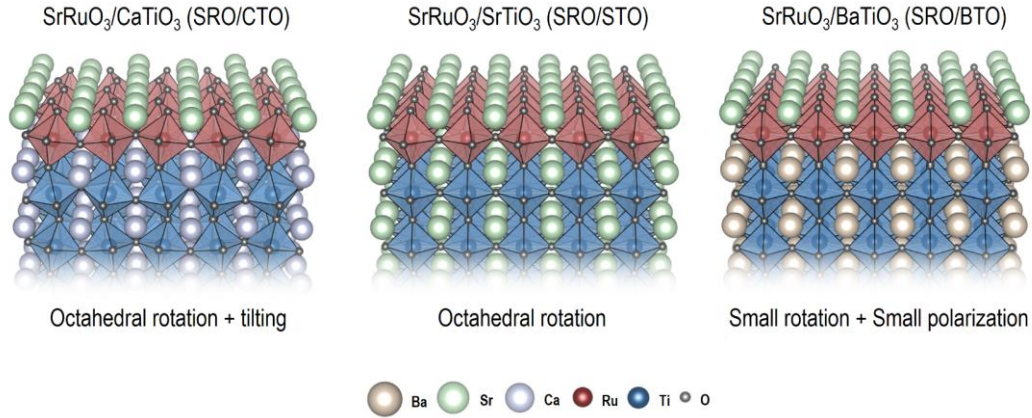


Figure 4.10 Schematic description of the interface control of the octahedral distortion in monolayer $\text{SrRuO}_3/\text{ATiO}_3$ (001) heterointerface ($A = \text{Ca}, \text{Sr}, \text{and Ba}$).

We checked the interfacial structural coupling at the SRO/ATO interface by STEM. To compare the SRO/CTO and ARO/STO interface, we carried out Annular bright field-STEM (ABF-STEM) analysis. Figure 4.11(a) shows the cross-sectional ABF-STEM image of the ATO/SRO/ATO interface. We observed an in-plane OOR at the SRO/CTO interface, but not in the SRO/STO interface. The result confirmed the expected $a^-b^+a^-$ ($a^0a^0c^-$) OOR pattern of the SRO layers grown on the CTO (STO) buffer layer.

Not only the ferroelectric polarization, but also the OOR could be modulated at the SRO/BTO heterointerface. In the presence of the ferroelectric polarization in the SRO layer [Fig. 4.11(b)], the competitive coupling between OOR and FE possibly suppresses the OOR distortion. Considering that the BTO has tetragonal symmetry as the STO does, the resulting OOR might be the $a^0a^0c^-$ pattern with a small OOR angle.

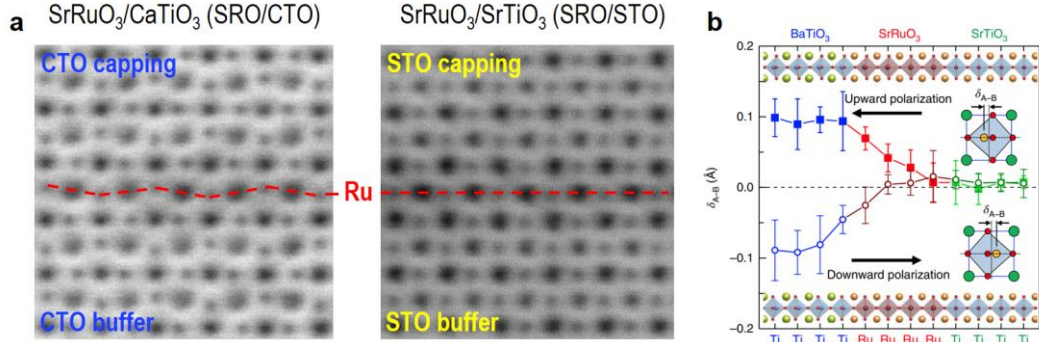


Figure 4.11 STEM analysis of the interface control of the octahedral distortion at monolayer SrRuO₃/ATiO₃ (001) heterointerface (A = Ca, Sr, and Ba). (a) ABF-STEM imaging of octahedral rotation. While SRO/CTO has octahedral tilt, SRO/STO do not shows it. (b) Ferroelectric proximity effect at the SrRuO₃/BaTiO₃ interface. Adapted from [34]

4.3.2 Crossover between Mott insulator, incoherent metal, and Fermi liquid in the monolayer SrRuO₃

We investigated the electronic structures of the atomically controlled, charging-free, and ultrathin SRO heterostructures. By suppressing and enhancing the OOR, we might control the bandwidth of the atomically thin SrRuO₃ and resulting electronic phases. Figure 4.12 shows the electronic structures of ultrathin SrRuO₃ layers grown on CaTiO₃, SrTiO₃, and BaTiO₃ buffer layers, respectively. To discuss the monolayer SRO first, an insulating gap opened on CaTiO₃ buffer layer, indicating that a bandwidth-controlled metal-insulator

transition. On BaTiO_3 , a strong quasi-particle peak emerged at the X point. This demonstrate a crossover from Mott insulator to Fermi liquid in the single-atomic-layer SrRuO_3 . Note that the effect of interface control weakens in the 2 and 3 uc SRO film, indicating how difficult it is to interfacially control the electronic structures. Even at the 3 uc thickness, SRO/STO and SRO/BTO exhibit almost identical Fermi surfaces.

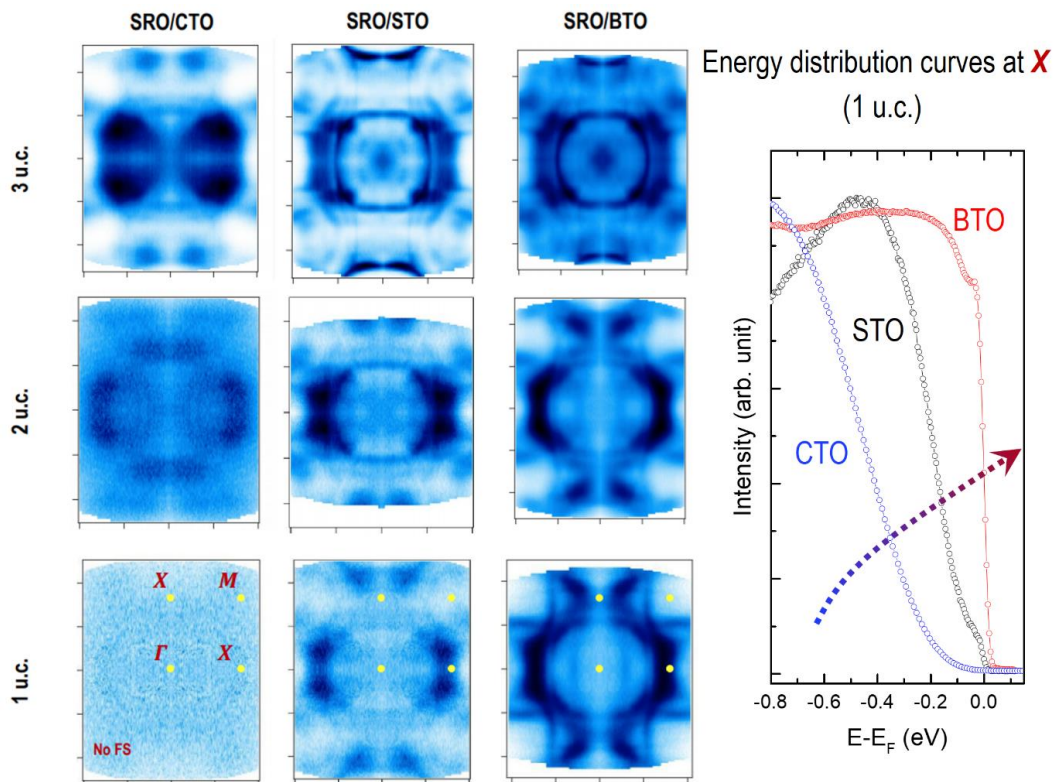


Figure 4.12 Crossover between Mott insulator, incoherent metal, and Fermi liquid at $\text{SrRuO}_3/\text{ATiO}_3$ (001) heterointerfaces ($A = \text{Ca}, \text{Sr}, \text{and Ba}$). Insulating gap (SRO/CTO), incoherent spectrum (SRO/STO), and quasi-particle peak (SRO/BTO) are shown.

4.4 Summary

2D materials and their applications are a rapidly growing field in contemporary condensed matter physics and materials science. This trend is becoming predominant not only for van der Waals materials but also for oxides. Even in recent years, free-standing oxides have been achieved, whose size is wafer-scale, and their crystallinity can be maintained down to the monolayer limit [35–37]. By demonstrating a metallic single-atomic-layer oxide, our work expands the scope of 2D oxides that has been limited to insulators so far.

The strong electronic correlation gives rise to highly tunable correlated electronic phases, which will be a distinguishing feature of 2D oxides in future research fields. We demonstrated the highly tunable electronic phases through the interface control of the electronic structures. We expect other emergent phases of oxides, such as unconventional superconductivity [38], to appear in a single-atomic-layer and thus pave the way to the two-dimensional correlated electronics.

References

- [1] A. Ohtomo and H. Y. Hwang, *Nature* **427**, 423 (2004).
- [2] H. Y. Hwang, *et al.*, *Nat. Mater.* **11**, 103 (2012).
- [3] P. Zubko, S. Gariglio, M. Gabay, P. Ghosez, and J.-M. Triscone, *Annu. Rev. Condens. Matter Phys.* **2**, 141 (2011).
- [4] R. Scherwitsl, *et al.*, *Phys. Rev. Lett.* **106**, 246403 (2011).
- [5] D. J. Groenendijk, *et al.*, *Phys. Rev. Lett.* **119**, 256403 (2017).
- [6] M. Huijben, *et al.*, *Phys. Rev. B* **78**, 094413 (2008).
- [7] C. R. Dean, *et al.*, *Nat. Nanotech.* **5**, 722 (2010).
- [8] A. K. Geim and I. V. Grigorieva, *Nature* **499**, 419 (2013).
- [9] Y. Cao, *et al.*, *Nature* **556**, 80 (2018).
- [10] Y. Cao, *et al.*, *Nature* **556**, 43 (2018).
- [11] M. Imada, A. Fujimori, and Y. Tokura, *Rev. Mod. Phys.* **70**, 1039 (1998).
- [12] E. Dagotto, *Rev. Mod. Phys.* **66**, 763 (1994).
- [13] Y. Tokura and Y. Tomioka, *J. Magn. Magn. Mater.* **200**, 1 (1999).
- [14] F. Kusmartsev, W. Wu, M. Pierpoint, and K. Yung, in *Applied Spectroscopy and the Science of Nanomaterials* (Springer, 2015) pp. 191–221.
- [15] P. W. Anderson, *Phys. Rev.* **109**, 1492 (1958).
- [16] J.-F. Ge, *et al.*, *Nat. Mater.* **14**, 285 (2015).
- [17] K. Yoshimatsu, *et al.*, *Science* **333**, 319 (2011).
- [18] D. Toyota, *et al.*, *Appl. Phys. Lett.* **87**, 162508 (2005).

- [19] P. King, *et al.*, Nat. Nanotech. **9**, 443 (2014).
- [20] H. K. Yoo, *et al.*, Phys. Rev. B **93**, 035141 (2016).
- [21] P. Schutz, *et al.*, Phys. Rev. Lett. **119**, 256404 (2017).
- [22] B. Kim, *et al.*, Phys. Rev. Lett. **101**, 076402 (2008).
- [23] M. Uchida, *et al.*, Phys. Rev. Lett. **106**, 027001 (2011).
- [24] A. P. Mackenzie and Y. Maeno, Rev. Mod. Phys. **75**, 657 (2003).
- [25] D. Shai, *et al.*, Phys. Rev. Lett. **110**, 087004 (2013).
- [26] H. Iwasawa, *et al.*, Phys. Rev. Lett. **105**, 226406 (2010).
- [27] A. Damascelli, Z. Hussain, and Z.-X. Shen, Rev. Mod. Phys. **75**, 473 (2003).
- [28] G. Koster, *et al.*, Rev. Mod. Phys. **84**, 253 (2012).
- [29] Y. J. Chang, *et al.*, Phys. Rev. Lett. **103**, 057201 (2009).
- [30] E. Ko, *et al.*, Phys. Rev. Lett. **98**, 226401 (2007).
- [31] H. J. Lee, C. H. Kim, and A. Go, Phys. Rev. B **102**, 195115 (2020).
- [32] Y. Shimakawa, *et al.*, Nat. Mater. **15**, 432–437 (2016).
- [33] S. H. Chang, *et al.*, Phys. Rev. B **84**, 104101 (2011).
- [34] L. Wang, *et al.*, Nat. Mater, **17**, 1087 (2018).
- [35] D. Lu, *et al.*, Nat. Mater. **15**, 1255 (2016).
- [36] H. S. Kum, *et al.*, Nature **578**, 75 (2020).
- [37] D. Ji, *et al.*, Nature **570**, 87 (2019).
- [38] Y. K. Kim, *et al.*, Science **345**, 187 (2014).

Chapter 5

Conclusion

We manipulated the octahedral rotation of perovskite oxides and their physical properties in the high-quality epitaxial heterostructures prepared by pulsed laser deposition. Both the angle and pattern of the oxygen octahedral rotation (OOR) were substantially effective in engineering the correlated electron systems and realizing exotic phases.

First, we stabilized a hidden-in-bulk ferroelectricity of CaTiO_3 using geometric constraint at room-temperature. Despite the ferroelectric instability, the bulk CaTiO_3 has only exhibited a paraelectric phase down to 0 K. It is due to the presence of competitive structural coupling between the ferroelectricity and the OOR, in its OOR pattern of $a^-b^+a^-$. We theoretically surveyed nonequilibrium OOR patterns of CaTiO_3 and found that the metastable $a^-a^-a^-$ pattern can accommodate ferroelectricity with a moderate energy cost. We selectively stabilized the $a^-a^-a^-$ OOR pattern of CaTiO_3 on the LaAlO_3 (111) substrate whose equilibrium OOR pattern is $a^-a^-a^-$. It was possible because of the strong interfacial octahedral connectivity with the LaAlO_3 and a unique 3-fold symmetry of the (111) surface. Scanning transmission electron microscopy combined with deep-neural-network analysis provided atomic-scale visualization of the OOR pattern. The analysis revealed a

close correlation between the OOR pattern and electric polarization in the $\text{CaTiO}_3/\text{LaAlO}_3$ heterostructures. Using piezoresponse force microscopy, we demonstrated that the observed electric polarization was switchable and stable at room-temperature.

Second, we presented tunable electronic phases of atomically thin SrRuO_3 films through the interfacial octahedral connectivity. The interfacial modulation of electronic structure has been unexplored due to the experimental difficulties. The major challenge was the absence of oxide electronic systems which is thin enough to observe the interface effect. We designed high-quality charging-free ultrathin $\text{SrRuO}_3/\text{SrTiO}_3$ (001) heterostructures to investigate the low-dimensional electronic phases and the interfacial modulation of the electronic structures. In the charging-free ultrathin heterostructures, we were able to investigate the intrinsic electronic structures via angle-resolved photoemission spectroscopy. Bulk SrRuO_3 is an itinerant ferromagnet. The electronic ground state of the atomically thin SrRuO_3 film has been controversial because of the experimental difficulties. For the first time, we clarified that SrRuO_3 can have a metallic electronic structure down to the monolayer limit. We observed the simultaneous suppression of quasi-particle peak and itinerant ferromagnetism below the three-unit-cell thickness. Systematic spectroscopic and theoretical analysis indicate that the monolayer $\text{SrRuO}_3/\text{SrTiO}_3$ (001) is indeed a Hund's metal where a quasi-particle is disturbed by spin fluctuation. Furthermore, using CaTiO_3 and BaTiO_3 buffer layer, we enhance or suppress the OOR of atomically thin SrRuO_3 layers. Depending on the buffer layers, remarkable changes in the electronic structures were observed, and the effect became more

pronounced in the reduced thickness. In the monolayer limit, the interfacial modulation of electronic structures was maximized, and the phases of the monolayer SrRuO₃ shows a crossover between the Fermi liquid, Hund's metal, and Mott insulator.

Our work emphasizes that heteroepitaxial engineering is remarkably effective for controlling the OOR and the associated physical properties. The nonequilibrium OORs give rise to the emergence of intriguing quantum phases in strongly correlated electron systems.

Publication List

1. **Jeong Rae Kim**, Byungmin Sohn, Choong Hyun Kim, Sangmin Lee, Sungsoo Hahn, Donghan Kim, Younsik Kim, Miyoung Kim, Changyoung Kim, Tae Won Noh, “Demonstration of controllable electronic structures at oxide interfaces”, *in preparation*.
2. Byungmin Sohn, **Jeong Rae Kim**, Choong Hyun Kim, Sangmin Lee, Sungsoo Hahn, Donghan Kim, Younsik Kim, Miyoung Kim, Tae Won Noh, Changyoung Kim, “Observation of a metallic single-atomic-layer oxide”, *in preparation*.
3. Chang Jae Roh, **Jeong Rae Kim**, Sungjoon Park, Yeong Jae Shin, Bohm-Jung Yang, Tae Won Noh, Jong Seok Lee, “Nonlinear optical characterization of surface and interface crystalline symmetries of SrRuO₃ thin films”, under review in *Applied Surface Science*.
4. Jihwan Jeong, Junsik Mun, Saikat Das, Jinkwon Kim, **Jeong Rae Kim**, Wei Peng, Miyoung Kim, Tae Won Noh, “Growth and atomically resolved polarization mapping of ferroelectric Bi₂WO₆ thin film”, *ACS Applied Electronic Materials*, in press.
5. **Jeong Rae Kim**, Jinhyuk Jang, Kyoung-June Go, Se Young Park, Chang Jae Roh, John Bonini, Jinkwon Kim, Han Gyeol Lee, Karin M. Rabe, Jong Seok Lee, Si-Young Choi, Tae Won Noh, Daesu Lee, “Stabilizing hidden room-temperature ferroelectricity via a metastable atomic distortion pattern”, *Nature Communications* **11**, 4944 (2020).

6. Chang Jae Roh, Myung-Chul Jung, **Jeong Rae Kim**, Kyoung-June Go, Jinkwon Kim, Ho Jun Oh, Young-Ryun Jo, Yeong Jae Shin, Jeong Gi Choi, Bong-Joong Kim, Do Young Noh, Si-Young Choi, Tae Won Noh, Myung Joon Han, Jong Seok Lee, “Polar metal phase induced by oxygen octahedral network relaxation in oxide thin films”, *Small* **16**, 2003055 (2020).
7. Hanyoung Ryu, Yukiaki Ishida, Bongju Kim, **Jeong Rae Kim**, Woo Jin Kim, Yoshimitsu Kohama, Shusaku Imajo, Zhuo Yang, Wonshik Kyung, Sungsoo Hahn, Byungmin Sohn, Inkyung Song, Minsoo Kim, Soonsang Huh, Jongkeun Jung, Donghan Kim, Tae Won Noh, Saikat Das, Changyoung Kim, “Electronic band structure of (111) SrRuO₃ thin films: An angle-resolved photoemission spectroscopy study”, *Physical Review B* **102**, 041102(R) (2020).
8. Sung Min Park, Bo Wang, Tula Paudel, Se Young Park, Saikat Das, **Jeong Rae Kim**, Eun Kyo Ko, Han Gyeol Lee, Nahee Park, Lingling Tao, Dongseok Suh, Evgeny Tsymbal, Long-Qing Chen, Tae Won Noh, Daesu Lee, “Colossal flexoresistance in dielectrics”, *Nature Communications* **11**, 2586 (2020).
9. Han Gyeol Lee, Lingfei Wang, Liang Si, Xiaoyue He, Daniel G. Porter, **Jeong Rae Kim**, Eun Kyo Ko, Jinkwon Kim, Sung Min Park, Bongju Kim, Andrew Thye Shen Wee, Alessandro Bombardi, Zhicheng Zhong, Tae Won Noh, “Atomic-scale metal-insulator transition in SrRuO₃ ultrathin films triggered by surface termination conversion”, *Advanced Materials* **32**, 1905815 (2020).
10. Seung Ran Lee, Lkhagvasuren Baasandorj, Jung Won Chang, In Woong Hwang,

- Jeong Rae Kim**, Jeong-Gyu Kim, Kyung-Tae Ko, Seung Bo Shim, Min Woo Choi, Mujin You, Chan-Ho Yang, Jinhee Kim, Jonghyun Song, “First Observation of Ferroelectricity in ~1 nm Ultrathin Semiconducting BaTiO₃ films”, *Nano Letters* **19**, 2243 (2019).
11. **Jeong Rae Kim**, Jiyeon N. Lee, Junsik Mun, Yoonkoo Kim, Yeong Jae Shin, Bongju Kim, Saikat Das, Lingfei Wang, Miyoung Kim, Mikk Lippmaa, Tae Heon Kim, Tae Won Noh, “Experimental realization of atomically flat and AlO₂-terminated LaAlO₃ (001) substrate surfaces”, *Physical Review Materials* **3**, 023801 (2019).
 12. Lingfei Wang, Rokyeon Kim, Yoonkoo Kim, Choon H. Kim, Sangwoon Hwang, Myung Rae Cho, Yeong Jae Shin, Saikat Das, **Jeong Rae Kim**, Sergei V. Kalinin, Miyoung Kim, Sang Mo Yang, Tae Won Noh, “Electronic-Reconstruction-Enhanced Tunneling Conductance at Terrace Edges of Ultrathin Oxide Films”, *Advanced Materials* **29**, 1702001 (2017).
 13. Yeong Jae Shin, Lingfei Wang, Yoonkoo Kim, Ho-Hyun Nahm, Daesu Lee, **Jeong Rae Kim**, Sang Mo Yang, Jong-Gul Yoon, Jin-Seok Chung, Miyoung Kim, Seo Hyoung Chang, Tae Won Noh, “Oxygen Partial Pressure during Pulsed Laser Deposition: Deterministic Role on Thermodynamic Stability of Atomic Termination Sequence at SrRuO₃/BaTiO₃ Interface”, *ACS Applied Materials & Interfaces* **9**, 27305 (2017).
 14. Yeong Jae Shin, Yoonkoo Kim, Sung-Jin Kang, Ho-Hyun Nahm, Pattukkannu Murugavel, **Jeong Rae Kim**, Myung Rae Cho, Lingfei Wang, Sang Mo Yang, Jong-

Gul Yoon, Jin-Seok Chung, Miyoung Kim, Hua Zhou, Seo Hyoung Chang, Tae Won Noh, "Interface Control of Ferroelectricity in an SrRuO₃/BaTiO₃/SrRuO₃ Capacitor and its Critical Thickness", *Advanced Materials* **29**, 1602795 (2017).

15. Seungwoo Song, Hyeon Han, Hyun Myung Jang, Young Tae Kim, Nam-Suk Lee, Chan Gyung Park, **Jeong Rae Kim**, Tae Won Noh, James F. Scott, "Implementing Room-Temperature Multiferroism by Exploiting Hexagonal-Orthorhombic Morphotropic Phase Coexistence in LuFeO₃ Thin Films", *Advanced Materials* **28**, 7430 (2016) .
16. Lingfei Wang, Myung Rae Cho, Yeong Jae Shin, **Jeong Rae Kim**, Saikat Das, Jong-Gul Yoon, Jin-Seok Chung, Tae Won Noh, "Overcoming the Fundamental Barrier Thickness Limits of Ferroelectric Tunnel Junctions through BaTiO₃/SrTiO₃ Composite Barriers", *Nano Letters* **16**, 3911 (2016).

국문 초록

산소 팔면체의 회전은 페로브스카이트 산화물이라고하는 물질 군에서의 근본적인 구조 변형이다. 이 산소 팔면체 회전은 페로브스카이트 산화물이 다양한 전이 금속 이온을 수용할 수 있도록 하여, 큰 범위의 강상관 전자 상을 형성한다. 이러한 강상관계 물질에서 전하, 스핀, 궤도 및 격자 자유도 간의 강력한 상호 작용은 관련 물리학을 연구함에 있어서 산소 팔면체 회전을 결정적인 요소로 만든다. 더 나아가, 산소 팔면체 회전의 정교한 조작을 통해 전이금속의 제어가능한 물성을 구현할 수 있음을 암시한다. 이 학위논문은 에피택시얼 페로브스카이트 산화물 이중구조에서 산소 팔면체 회전 및 관련 물성의 제어를 실험적으로 보여준다.

페로브스카이트 산화물로 구성된 인공 이중 구조는 광범위한 발현현상과 가능성을 가져왔다. 이 다방면으로 유용한 시스템은 다른 물질과 잘 정의된 계면을 형성할 수 있는 ABO_3 페로브스카이트 구조의 높은 집적도에서 비롯된다. 산소 팔면체 회전은 3차원적으로 연결된 팔면체의 집합적 움직임이기 때문에 이 산화물 계면에서는 강한 팔면체 연결성이 예상된다. 우리는 산소 팔면체 회전을 제어하기 위해 이 계면 팔면체 연결성을 이용하여 새로운 강유전성과 제어 가능한 전자 구조를 실험적으로 구현하고자 한다.

산소 팔면체 회전은 23 가지 가능한 패턴이 있지만 몇 개의 회전 패턴 만이 덩치 시료에서 존재한다. 이러한 경향은 페로브스카이트 산화물의 가능한 특성 및 기능의 범위를 제한하고, 이를 극복하기 위해 비평형 산소 팔면체 회전 패턴의 활용이 필요하다. 이 학위논문에서는 인공적으로 설계된 준 안정 산소 팔면체 회전 패턴이 CaTiO_3 에서 강한 실온 강유전성을 유도한다는 것을 보여준다. 먼저, 밀도범함수 이론을 기반으로 CaTiO_3 의 10 가지 가능한 비평형 산소 팔면체 회전 패턴을 조사하고, 그중 강유전성과 협동하는 준 안정 산소 팔면체 회전 패턴을 발견했다. 우리는 에피택시얼 이중구조의 기하학적 설계를 사용하여 CaTiO_3 의 목표 산소 팔면체 회전 패턴을 안정화했다. 심층 신경망 분석과 결합된 원자 단위 시각화 방법으로 준 안정 산소 팔면체 회전 패턴과 전기 자발 분극 간의 밀접한 상관 관계를 확인했다. 이 전기 자발 분극은 상온에서 반전 가능하고 안정적이었으며, 이는 산소 팔면체 회전 패턴의 제어가 새로운 강유전성 물질을 만들 수 있음을 보여준다.

산화물 계면의 전자 구조로의 큰 관심에도 불구하고 직접적인 실험 규명은 이루어 지지 않았는데, 이를 극복하기 위해선 산화물 계면의 전자 구조를 연구하기 위한 새로운 실험 방법의 개발이 필요하다. 우리는 이러한 계면 제어 효과가 공간적으로 제한된 규모를 가질 것이라고 생각하고, 먼저 수 원자 층 단위 두께의 얇은 전자 전이 금속 산화물 이중 구조를 탐색하였다.

지금까지의 보고들에서는 전이 금속 산화물 박막은 단일 원자 층 두께로 제한될 때 부도체 특성을 보여왔다. 이는 전자 상이 본질적으로 부도체 이기 때문일 뿐만 아니라 도체 특성을 단일 원자 층 한계까지

유지하는 실험적 어려움 때문이기도 하다. 우리는 원자단위 켈프기와 각분해 광 전자 분광법을 결합하여 단일 원자 층 SrRuO_3 가 강한 상관관계를 가지고 있는 금속이라는 것을 발견했다. 체계적인 분석을 통해 전자 상과 자성 사이의 밀접한 상관 관계를 규명하였다.

SrRuO_3 박막의 전자 구조를 단층까지 규명한 후, 우리는 전이 금속 산화물 이중 구조에서 전자 구조의 계면 제어를 실험적으로 시연한다. 우리는 SrRuO_3 층에 다른 구조 변형을 부여하는 BaTiO_3 , SrTiO_3 및 CaTiO_3 의 부도체 완충 층을 사용했다. 두 원자 층 두께 이상에서는 SrRuO_3 필름의 전자 구조에서 큰 변화가 관찰되지 않았지만, 두개와 단일 원자 층 두께에서 계면에 의한 전자 구조의 변화를 관측했다. 단일 원자 층 한계의 2 차원 전자 구조에서는 Fermi-liquid, incoherent metal 그리고 Mott insulator 전자상의 교차가 이루어 졌다.

주요어: 페로브스카이트 산화물, 산소 팔면체 회전, 강상관계 물질, 산화물 이중구조, 펄스 레이저 증착법, 강유전성, 전자구조

학번: 2015-20322